Expedition 314 Site C0006[1]

Expedition 314 Scientists[2]

Chapter contents

Background and objectives

Integrated Ocean Drilling Program (IODP) Site C0006 (proposed Site NT1-03) (Figs. F1, F2) is located at the frontal thrust of the Nankai accretionary prism near the trench axis. Drilling targeted the main frontal thrust at an estimated depth of ~700 meters below seafloor (mbsf), as well as subsidiary faults and deformed sediments in the hanging wall above that zone and a footwall zone of strong reflectors likely caused by coarse turbiditic trench fill sediments. Overall objectives of drilling this site with logging-while-drilling (LWD)-measurement-while-drilling (MWD) instruments were to characterize the lithology, deformation, stress state, and physical properties of the hanging wall rocks and frontal thrust fault zone. LWD drilling during Expedition 314 contributed in situ resistivity, gamma ray, and ultrasonic caliper logs, as well as borehole imagery for this characterization. Unfortunately, no neutron porosity or lithodensity logs were obtained because of the inability to run a radioactive source at this site, and the sonic tool failed to record useful data for most of the interval below 274 m LWD depth below seafloor (LSF) because of loss of the MWD turbine power system.

Based on seismic data and submersible dive studies (Ashi et al., 2002), this frontal thrust system was predicted to have placed moderately consolidated clastic rocks over weak and unlithified upper Quaternary trench section clastic sediments. However, at the final location chosen for Site C0006, it is not clear whether the same older section sampled by submersible is in the thrust sheet or if it is exclusively composed of uplifted trench wedge. Detailed analysis of seismic data suggests that substantial footwall protothrust deformation exists a few hundred meters below the main frontal thrust fault at this site location, implying the existence of a deeper décollement and that strain decoupling is not total across this fault. Reflection amplitude of this fault plane is variable near this site, but generally it is a negative polarity reflector. Characterization of physical properties across the frontal thrust zone, as well as the many subsidiary faults imaged in the thrust sheet, were primary objectives of drilling this site; however, the lack of porosity and velocity data has hampered this effort. Nevertheless, resistivity imaging and other data provides extensive documentation of fracture and stress orientation, lithology, and possible fault repetition of strata.

[1] Expedition 314 Scientists, 2009. Expedition 314 Site C0006. *In* Kinoshita, M., Tobin, H., Ashi, J., Kimura, G., Lallemant, S., Screaton, E.J., Curewitz, D., Masago, H., Moe, K.T., and the Expedition 314/315/316 Scientists, *Proc. IODP,* 314/315/316: Washington, DC (Integrated Ocean Drilling Program Management International, Inc.). doi:10.2204/iodp.proc.314315316.118.2009
[2] Expedition 314/315/316 Scientists' addresses.

doi:10.2204/iodp.proc.314315316.118.2009

Pilot Hole C0006A was drilled with MWD-annular-pressure-while-drilling (APWD) and gamma ray tool string to total depth (TD) of 885.5 m LSF, and Hole C0006B was drilled to the same TD with the full LWD tool string but without any radioactive source in the adnVISION tool. Drilling was smooth; however, real-time MWD communication was lost at 274 m LSF, as well as the power from the MWD turbine. LWD tools recorded data in memory mode on battery power; however, sonic source transducers were negatively affected and sonic data were of very poor to unusable quality from 274 m LSF to TD (885.5 m LSF). Drilling was initially planned to 950 mbsf but was terminated at 885 mbsf. MWD data showed that drilling was penetrating thick sandy sequences and conditions were deteriorating below ~800 m LSF. Judging that drilling had passed through the main fault reflector position at <700 m, we decided the objective had been met and the hole was terminated.

Operations

Hole C0006A

The summary of operations in Hole C0006A is shown in Table **T1.** The drill string was spaced out in preparation for drilling, and the Schlumberger MWD and APWD tools were tested in preparation for drilling pilot Hole C0006A (initial target depth = 950 m LSF; drilled to 885.5 m LSF). The bottom-hole assembly (BHA) included polycrystalline diamond compact (PDC) bit, a crossover sub, MWD (PowerPulse) and APWD tools, a stabilizer and nine 6¾ inch drill collars, and one jar (see Fig. **F1** in the "Expedition 314 methods" chapter; Table **T2**). Tools were assembled and we started running into hole between 0040 and 2045 h on 9 November 2007. Because of the high current, all pipe connections were checked while running in. Because water depth was deeper than the remotely operated vehicle's (ROV's) capability (3000 m), the hole was positioned based on ship position. After spud-in, drilling and MWD logging operations began at 0015 h on 10 November. Based on the cumulative length of drilling pipe, the seafloor depth was estimated to be 3903.5 m (3903.5 m drillers depth below rig floor [DRF]).

A time version of the surface drilling parameters and downhole MWD measurements of equivalent circulating density (ECD), average annular pressure (APRS), and gamma ray values (GR_RAB) is given in Figure **F1.** The hole was jetted-in to 3954 m DRF (50.5 m LSF) with a minimal (<2 kkgf) weight on bit (WOB) and standpipe pressure (SPPA). Surface pump flow was set to 520 gpm. After 50.5 m LSF, bit rotation (CRPM) was progressively increased to 80–100 rpm to 150 m LSF and then stabilized at ~120 rpm to TD (885.5 m LSF). Increase in CRPM was concomitant with increased SPPA and surface pump flow. A first wiper trip was conducted between 4210 and 4060 m DRF (306.5–156.5 m LSF; 1415–1530 h on 10 November) and a second wiper trip was conducted between 4504 and 4364 m DRF (600.5–460.5 m LSF; 0500–0545 h on 11 November). Drilling progressed smoothly with an average rate of penetration (ROP) of ~30 m/h. Normal hydrostatic increase with depth was observed on APRS and ECD. Annular temperature (ATMP) also gradually increased to 12°C at the bottom of the hole. Total depth of 885.5 m LSF was reached at 2045 h on 11 November, after 45 h of drilling operations. The BHA was then pulled out of the hole and the drill bit cleared the seafloor at 2400 h on 11 November. The drill bit was recovered on the rig floor at 1015 h on 12 November.

Hole C0006B

The summary of operations in Hole C0006B is shown in Table **T1.** Hole C0006B was spudded at 0045 h on 13 November 2007. The LWD-MWD drilling/logging operations were conducted from the seafloor (3900.0 m DRF) to TD of 4785.5 m DRF (885.5 m LSF). As water depth exceeded the 3000 m ROV limitation, the position of the hole was determined by the position of the ship. At the time of spud-in, ship position was 33°01.6350′N, 136°47.6390′E.

Operations began with the makeup of the BHA (from 1115 to 2000 h on 12 November). The BHA included a PDC bit, various subs, LWD tools, one mechanical jar, nine 6¾ inch drilling collars, and an extra crossover sub to connect the BHA to the drill pipes (Table **T3**). The LWD tools (6¾ inch [17.15 cm] collars) included geoVISION, sonicVISION, MWD (PowerPulse), adnVISION (caliper-only mode), and seismicVISION tools (see Fig. **F1** in the "Expedition 314 methods" chapter). Seafloor was tagged at 3900 m DRF (3871.5 meters below sea level) at 0045 h on 13 November (Table **T1**).

Hole C0006B was jetted-in with an initial pump rate of 500 gpm to ~40 m LSF. Real-time communication with the tools was poor because the pump rate was limited in the slipping mode interval to reduce washout. Graphic representation of drilling parameters and the gamma ray log is given in Figures **F3** and **F4.** Real-time communication with the LWD tools was lost at 1800 h on 13 November (274 m LSF) because the mud pulse telemetry system failed. Drilling progressed smoothly at a constant ROP of 40 m/h. CRPM progressively increased from 80 rpm (40 m LSF) to 100–120 rpm to the end of operation. Pump flow increased to 700 gpm, and SPPA was mostly maintained below 15 MPa. Major reaming opera-

tions were conducted during drilling as a result of an observed increase in hole deviation (~5° at 240 m LSF). A wiper trip was conducted from 4502 to 4350 m DRF (602.5–450.5 m LSF) at 0330–0415 h on 14 November. The target depth of 885.5 m LSF was reached at 1645 h on 14 November. The hole was killed by circulating heavy mud, and tools were pulled out at 1900 h. After the drill string was above the seafloor, the drilling equipment and derrick were checked before continuing pullout. LWD tools were recovered on the rig floor at 1715 h on 15 November, and all data successfully downloaded.

Transit to Hole C0001E

After pulling out of Hole C0006B, the D/V *Chikyu* moved ~ 14 nmi to Site C0001 with an average speed of 3.5 kt at 1700 h on 15 November 2007 and arrived at the location at 2100 h.

Data and log quality

Hole C0006A

Available data

Hole C0006A was drilled with MWD-APWD tools. All data were sent to the surface through the drilling fluid telemetry system (see Fig. **F3** in the "Expedition 314 methods" chapter). At the end of the drilling operation, time and depth information were merged and data was processed following the data flow presented in Figure **F3** in the "Expedition 314 methods" chapter. Retrieved data include

1. Surface drilling control parameters: ROP, hook load (HKLD), surface weight on bit (SWOB), SPPA;
2. Downhole drilling parameters: drill bit (collar) rotation (CRPM_RT), PowerPulse turbine rotation speed (TRPM_RT);
3. Annular pressure data: average annular pressure (APRS_MWD) and temperature (ATMP_MWD) and equivalent circulating density (ECD_MWD); and
4. Gamma ray log (GR_RAB) for further depth correlation over interval 0–879 m LSF (3903.5–4782.5 m DRF).

Depth shift

For this hole, the mudline (seafloor) was identified from the first break in the gamma ray log (GRM1) found at 3903.5 m DRF (Fig. **F5**) while tagging the seafloor without ROV monitoring. GRM1 is particularly noisy at the seafloor interface because the fast ROP (jet-in) in the unconsolidated formation is incompatible with a reliable statistical count of the radioactive elements of the formation and possible flow of mud around the bit. The depth-shifted version of the surface and downhole drilling data and downhole ECD, APRS, and GRM1 is given in Figure **F6.** To help connect the time and depth version of the data, the time-depth relationship for Hole C0006A is given in Figure **F7.**

Logging data quality

Except for the MWD tool GRM1 log, which is directly related to the formation properties (lithology), all other logs are direct surface drilling and downhole measurements. APRS, ATMP, and ECD derived from APRS show an expected increase with depth. As GRM1 has a high depth of investigation, it is considered reliable despite the lack of hole shape (caliper) data. No repeat data were available in this hole; however, this GRM1 log is well correlated with the gamma ray log (GR_RAB) of the geoVISION resistivity tool (GVR) from Hole C0006B. Minor depth discrepancies can be attributed to lateral variations/heterogeneities between these two holes (Fig. **F8**).

Hole C0006B

Available data

Hole C0006B was drilled with LWD-MWD-APWD tools. As in Hole C0004A, the adnVISION tool was deployed to obtain ultrasonic caliper data. Despite the loss of real-time communication with the LWD tools (1500 h on 13 November 2007; 345.2 m LSF), drilling operations were conducted to TD (885.5 m LSF) and memory data were successfully downloaded.

Depth shift

For Hole C0006B, the mudline (seafloor) was identified from the first break in the gamma ray log (GR) and resistivity logs (RES_RING, RES_BIT, RES_BD, RES_BM, RES_BS) at 3899.5 m DRF, showing a discrepancy with drillers depth by 0.5 m (3900.0 m DRF) (Fig. **F9**). Uncertainty in picking the mudline is clearly within ±1 m because of the washing out of the top few meters of the unconsolidated formation by drilling fluid and the resultant mixing (formation suspension) at the mudline interface, blurring gamma ray and resistivity readings.

For Hole C0006B, the depth-shifted version of the main drilling data and geophysical logs are given in Figures **F8** and **F10,** respectively. Figure **F11** presents the time-depth relationship linking the time (Fig. **F2**) and depth (Figs. **F8, F10**) version of the data in Hole C0006B.

Logging data quality

Figures F8 and F10 show the quality control logs for Hole C0006B LWD data. The target ROP of 30 m/h (±5 m/h) was generally achieved to TD (see "Hole C0006B" in "Operations"). This ROP was sufficient to record 1 sample every 4 cm over the majority of the hole. SPPA increased with depth from 10 to 18 MPa, and no noticeable change in APRS and ECD was observed until the loss of the real-time communication with the LWD-APWD tools. Hole deviation quickly reached 5° (250 m LSF), but memory data show that hole deviation stabilized with depth, remaining close to 5° at 885.5 m LSF.

Hole conditions are highly variable with depth. Sonic caliper values from the adnVISION tool that should be 8.5 inches (21.6 cm) for a perfect in-gauge hole instead show values >10 inches (25.4 cm) for the upper depth interval (0–200 m LSF), the lower depth interval (710–855 m LSF [last caliper reading]), and a few localized (approximately meter scale) washouts. All these depth intervals are characterized by low gamma ray counts suggesting caving in sand-rich layers.

Comparison between deep button (RES_BD) and shallow button (RES_BS) resistivity values shows that drilling fluid invasion is concomitant with low gamma ray depth intervals in spite of the short time after bit measurements. Combined with hole conditions and caliper information, these layers can possibly be interpreted as permeable sand-rich layers.

Because of the limited time available before the end of the cruise, sonicVISION data for Hole C0006B were processed postcruise by the Schlumberger Data Consulting Specialist. The depth interval of usable processed data was limited by the failure of real-time communication and powering of the sonic tool (1500 h on 13 November 2007; 345.2 m LSF) and the possible damage of the transmitter. At the time real-time communication failed, the sonic tool switched from turbine mode to battery mode. Because of the low downhole temperature (~3°C), the batteries did not provide enough voltage to the transmitter, therefore limiting the available energy to excite the formation. Possible damage of the transmitter resulting from improper stabilization of the tool and/or severe drilling conditions (stick-slip or shocks) may have also impaired data quality. As a result, only the uppermost 160 m has been processed by combining the results of wide and leaky-P processing, attempting to select wide results when available. Quality control analysis of sonic data is based on examination of plots showing sonic waveforms and slowness coherence images for common receiver data and common source data. From 36 to 160 m LSF, sonic data quality is moderate; discontinuous transit times have been picked using mostly wide processed data. Above 36 m LSF, formation arrival can not be distinguished from mud arrival (Table T4).

Overall quality of the resistivity images used in structural interpretation is very good (Fig. F10; Table T5). The following descriptions of logging units include areas of apparent artifacts probably reflecting hole or tool conditions and not real geology. This assessment was based on the shallow level of investigation of the GVR tool, displayed as a static, not a dynamically renormalized, image.

Log characterization and lithologic interpretation

Log characterization and identification of logging units

Site C0006 logging units were characterized from visual inspection of gamma ray, resistivity, and caliper log responses (Fig. F1). Resistivity images were used to define finer scale characteristics within the units. Four primary logging units were defined based on the variability of log responses (Tables T6, T7).

Logging Unit I (0–197.8 m LSF) is characterized by a gradual increasing trend starting at 52 m LSF and variable gamma ray values from 20 to 70 gAPI. This logging unit is also characterized by high-amplitude fluctuation of ring (1–3 Ωm), shallow (0.5–2 Ωm), and deep (1–2.5 Ωm) button resistivity values. Ring and deep button resistivity values in this logging unit increase with depth from 0.5 to 2.0 Ωm. Caliper values show high-frequency and high-amplitude oscillation and the baseline of borehole diameter is consistently large (10–11 inches) over this logging unit (Fig. F1).

Logging Unit II (197.8–428.3 m LSF) is characterized by a gradual increasing trend of gamma ray baseline with depth from 60 to 80 gAPI. Four thick intervals of low gamma ray values (<30 gAPI) are observed at 216–223, 238–245, 298–305, and 330–335 m LSF (Fig. F1). Ring and bit resistivity logs exhibit a constant baseline trend between 1.8 and 2.0 Ωm, except for the interval 280–330 m LSF, which exhibits a variable trend from 1.5 to 2.5 Ωm. Ring and bit resistivity logs also exhibit four conductive intervals to 1.0 Ωm at the same intervals of low gamma ray values. Shallow and deep button resistivity logs show similar trends and four conductive intervals are sharply defined. This logging unit is also characterized by a decreasing trend of borehole diameter from 10 to 9 inches with distinct washouts as much as 14 inches in diameter corresponding to the low gamma ray intervals (Fig. F1).

Logging Unit III (428.3–711.5 m LSF) is defined as an interval of high-frequency and high-amplitude gamma ray fluctuations. This logging unit is divided into two subunits (Table T6). Logging Subunit IIIA (428.3–545.3 m LSF) is characterized by a gradual increasing trend in gamma ray baseline from 70 to 90 gAPI. Negative meter-scale spikes of gamma ray values to 50 gAPI are common within this subunit. All resistivity logs exhibit a near constant trend around 1.5 Ωm (Fig. F1).

Logging Subunit IIIB (545.3–711.5 m LSF) is also characterized by high-frequency and high-amplitude gamma ray log fluctuations. Gamma ray values are more variable (30–100 gAPI) than those found in logging Subunit IIIA (40–90 gAPI) and exhibit the highest values (up to 100 gAPI) in Hole C0006B. More than 20 spikes of low gamma ray values to 30 gAPI are observed in this subunit. Resistivity logs exhibit a variable trend between 1.0 and 2.5 Ωm, with increasing trends in resistivity observed over the intervals 594–652 and 656–710 m LSF. Borehole diameter shows nearly constant values (9 inches) at the upper part of this logging subunit and large variation from 9 to 14 inches below 652 m LSF. The base of logging Unit III is defined by a sharp decrease in gamma ray and resistivity values (Fig. F1).

Logging Unit IV (711.5 m LSF to TD) is characterized by the lowest gamma ray and resistivity values for this hole. The gamma ray log ranges between 20 and 50 gAPI except for the interval of high gamma ray values (up to 80 gAPI) at 712–730 m LSF. Resistivity logs exhibit a slight deceasing trend with depth from 1.0 to 0.5 Ωm. Resistivity logs show high-frequency oscillation over the interval 711.5–762 m LSF and decameter-scale cyclic variation over the lower part of this logging unit. Logging Unit IV is also characterized by high values and high-frequency oscillation of borehole diameter fluctuating between 10 and 14 inches (Fig. F1).

Figure F12 illustrates ring resistivity and gamma ray distributions for the logging units and subunits. The gamma ray log exhibits a trend of gradual increase from logging Unit I to Subunit IIIB, with extremely low values for logging Unit IV. Ring resistivity shows a broad range of values in logging Unit I and a gradual decreasing trend from logging Units II to IV. Figure F13 shows a cross-plot of gamma ray values versus ring resistivity. Logging Unit III is characterized by high gamma ray values. Logging Unit IV is characterized by low gamma ray and resistivity values.

Lithologic interpretation

Log responses in conjunction with resistivity-at-the-bit (RAB) images in Hole C0006B show lithologic characteristics and detailed sedimentary/structural features (Figs. F1, F14, F15).

Logging Unit I

Logging Unit I is characterized by an increasing baseline trend and oscillation of gamma ray and resistivity values. Resistivity logs and RAB images demonstrate clear decameter- to centimeter-scale alternating bedding. The caliper log shows significant washouts in logging Unit I resulting from the unconsolidated state. These log signatures suggest that the lithology of logging Unit I consists of unconsolidated and uncemented interbeds of sand and mud. Based on the interpretation of borehole images, the general trend of the bedding plane is westward dipping, which is obviously different than trends in lower logging units (Fig. F14).

Logging Unit II

Logging Unit II is characterized by higher values of gamma ray baseline with several prominent, ~5 m thick layers with low gamma ray values. This log character is interpreted as mudstone with major, thick sand layers. Fining-upward sequences in these sand layers are clearly seen in the RAB images as a transition from dark (conductive) at the base of the sequence changing gradually to light (more resistive) toward the sequence top. A similar trend is shown on gamma ray and resistivity logs (Fig. F15). The upper and lower pairs of sand layers are presumably stratigraphic repetition. However, these sand layers and the surrounding formations are not correlated with each other in a simple way because of the complexity of faulting (see **"Structural geology and geomechanics"** and **"Log-seismic correlation"**). Bedding dip and orientation patterns within this unit show variability (Fig. F14) that is likely the result of disruption of the original bedding caused by complex deformation.

Logging Unit III

Logging Unit III is characterized by a high gamma ray baseline with frequent thin low gamma ray layers. These log responses are interpreted as alternating beds of mudstone and sand. Thickness and frequency of coarse layers are quite different from those of logging Unit II. The gamma ray log also suggests that the sand/mud ratio in logging Subunit IIIB (sand-dominant facies) is larger than that formed in logging Subunit IIIA (mud-dominant facies) (Fig. F1).

Based on borehole image interpretation, a number of alternating bedding features are recognized but specific textures or sedimentary features are not clearly imaged. A general trend of bedding is northward and

southward dipping for logging Subunit IIIA and northward to northwestward dipping for logging Subunit IIIB (Fig. F14). Logging Subunit IIIA is relatively homogeneous and conductive. Logging Subunit IIIB is characterized by three decameter-scale resistive (light) intervals changing to conductive (dark) sediments with depth. These trends are consistent with gamma ray trends and are likely related to textural and compositional changes.

Logging Unit IV

Very low gamma ray values (lowest in Hole C0006B) suggest that the lithology of logging Unit IV is sand dominated. Borehole diameter is as large as that of logging Unit I, possibly caused by an unconsolidated/uncemented state. Based on borehole image interpretation, sedimentary structures and deformation features are not very clear because of the possible massive character of the formation and also washouts. A general trend of the bedding planes is northward dipping throughout the unit. This bedding structure is slightly different from that of logging Unit III (Fig. F14). All log responses suggest that the lithology of logging Unit IV is uncemented massive sand.

Based on the seismic section (see **"Log-seismic correlation"**), logging Unit IV is correlated to possible underthrust sediments. Although the lithologic contrast demonstrated by the abrupt decrease of gamma ray and resistivity logs is large between logging Units III and IV, deformation structures between the two logging units are poorly identified (see **"Structural geology and geomechanics"**) and the seismic and RAB structural interpretation places the likely main thrust fault ~50 m higher at 657 m LSF within logging Subunit IIIB.

Physical properties

The available data relevant to physical properties include five different sets of resistivity logs (bit; ring; and shallow, medium, and deep button) and sonic *P*-wave velocity. No neutron porosity (TNPH) or density (RHOB) data were recorded.

As at previous sites, additional analyses were conducted to produce porosity estimates derived from resistivity. In the process, the estimation of temperatures and formation factors were carried out.

Resistivity and estimated porosity

Resistivity logs

Figure F16 shows ring and bit resistivity measurements side by side and smoothed logs of shallow, medium, and deep button resistivity. A moving average using a 21-point (~3 m interval) window was used to smooth the resistivity values. Superposition of deep, medium, and shallow button resistivity measurements shows very good agreement between medium and deep button resistivities. Shallow button resistivity is significantly lower than the two other button resistivities in logging Units I and IV (Figs. F16, F17).

Based on bit resistivity, logging Unit I resistivity values generally increase from 1.1 to 2.0 Ωm and show an important excursion to higher resistivity values from 50 to 100 m LSF that includes a peak of resistivity of 2.6 Ωm at 85 m LSF. The trend of resistivity becomes fairly constant in logging Unit II where it varies slightly around 1.9 Ωm. Four excursions to low resistivity value are noticeable in this unit.

At the top of logging Subunit IIIA (from 429 to 460 m LSF), the trend is a decreasing one from 1.8 to 1.5 Ωm and increases again to 1.7 Ωm at 530 m LSF. The bottom of this subunit is marked by a sharp minimum of resistivity at 1.3 Ωm. The underlying logging subunit (IIIB) is characterized by alternating zones of higher and lower resistivity values. From 545 to 590 m LSF, resistivity values fluctuate around 1.7 Ωm with a minimum in resistivity (1.2 Ωm) at 560 m LSF. This zone ends on a decreasing step of resistivity (from 1.8 to 1.4 Ωm) and is followed by a zone of constant resistivity values (1.4 Ωm) from 590 to 615 m LSF. Below this zone, the trend of resistivity increases again to 2.1 Ωm at 640 m LSF, where a second decreasing step is observed (from 2.1 to 1.4 Ωm). This decreasing step is followed by a decreasing trend of resistivity (from 1.4 Ωm at 655 m LSF to 1.2 Ωm at 690 m LSF) and an increasing trend (from 1.2 Ωm at 690 m LSF to 1.7 Ωm at 710 m LSF). The boundary between logging Units III and IV is marked by a decreasing step of resistivity from 1.7 to 1.2 Ωm.

The trend of resistivity stays fairly constant (1.2 Ωm) in the uppermost 30 m of logging Unit IV. At 740 m LSF another decreasing step of resistivity is observed (from 1.2 to 0.9 Ωm), followed by a nearly constant trend of resistivity (0.9 Ωm). At 840 m LSF a final increasing step of resistivity is observed from 0.8 to 1.2 Ωm followed by a decreasing trend of resistivity reaching 0.75 Ωm at the bottom of the hole.

Estimation of temperature profile

The downhole temperature profile was estimated from a regional surface heat flow of 80 mW/m^2 (Kinoshita et al., 2003) and 2°C surface temperature. Thermal conductivity (k) was estimated from Ocean Drilling Program Leg 131 Site 808 data as $k = 1 + (z/800)$ for $z < 400$ m and $k = 1.5 + (z - 400)/2000$ for $z > 400$ m. The estimated temperature is 52°C at 886 m LSF.

Estimation of porosity from resistivity

Bit and ring formation factors have been calculated from resistivity logs and temperature-corrected seawater electrical resistivity. They were converted to porosity using Archie's law. In the absence of neutron porosity data to calibrate Archie's law parameters, the parameter values a = 1 and m = 2.4 were used. The values are the same as those at previously drilled Expedition 314 sites where these values were calibrated from comparison with log porosity data (neutron and density porosity). However, sand content at Site C0006, apparently much greater than that found at other sites, means that porosity and density estimates may be strongly affected by lithology, which is not accounted for in these calculations.

In logging Unit I, bit resistivity–derived porosity decreases from 85% at 0 m LSF to 51% at 50 m LSF (Fig. F18) and 41% at 86 m LSF. Resistivity-derived porosity then increases to 49% at 116 m LSF and decreases back to 40% at 197.8 m LSF at the boundary between logging Units I and II. In Unit II, resistivity-derived porosity decreases slowly to 38% at 428 m LSF, the transition with Unit III. In the uppermost 34 m of Unit III, resistivity-derived porosity increases to 41% at 462 m LSF and then decreases to 36% at 590 m LSF. At the base of Unit III, resistivity-derived porosity is 36% and jumps to 41% over 6 m at the transition with Unit IV. In Unit IV, resistivity-derived porosity begins by increasing to 48% at 762 m LSF. Resistivity-derived porosity then fluctuates around an average value of 46%. At 850 m LSF resistivity-derived porosity decreases to a low value of 39% before increasing back to 47% at 884 m LSF at the base of the hole. Again, caution is required in interpreting these values, as Unit IV is interpreted as being a much sandier lithology than the basis of calibration (see **"Log characterization and lithologic interpretation"**).

Estimation of density

Because of the absence of bulk density measurements, we made an estimation of bulk density from resistivity-derived porosity (Fig. F18). Resistivity-derived porosity was converted to density using standard methods (see **"Physical properties"** in the "Expedition 314 methods" chapter).

P-wave velocity

Because of a malfunction of the sonic tool at Site C0006, *P*-wave velocity data were measured only to 160 m LSF, which corresponds to sediments in most of logging Unit I (Fig. F19). In the uppermost 40 m, the measured *P*-wave velocity is indistinguishable from the mud arrival (~1500 m/s). At ~40 m LSF, velocity jumps to ~1750 m/s. Below this level, velocity appears to be nearly constant or slightly increasing. At the base of measurements (160 m LSF), velocity is measured at ~1860 m/s. Some velocity peaks are noted at 70, 94, 101, and 130–140 m LSF, which may be interpreted as clay-rich intervals where gamma ray values are relatively high (see **"Log characterization and lithologic interpretation"**).

Velocity and resistivity are generally in good agreement; high velocity zones correspond to high resistivity zones. This is clearly seen in the cross-plot between velocity and bit resistivity, in which their relationship is approximately linear (Fig. F20). The only exception is high-resistivity data (>2 m) in the interval between 80 and 90 m LSF. In this low–gamma ray sandy zone, velocities are low (~1700 m/s).

Structural geology and geomechanics

Very good quality borehole resistivity images provide information on orientation of bedding, fractures, and breakouts at Site C0006 (Fig. F21). In addition, the overall stratigraphic sequence and seismic reflection images allow interpretation of the structural geology.

Observations

Bedding

Bedding dips are shallow to moderate with most dips <45°. Bedding orientation is partitioned downhole with mostly westward dips above 198 m LSF (logging Unit I) (Figs. F21, F22). Dips below 428 m LSF (logging Units III and IV) are northwestward. Dips between 198 and 428 m LSF (logging Unit II) are diverse and do not meaningfully cluster.

Natural fractures and fractured zones

Fracture analysis from borehole images is primarily based on orientation, dip, and resistive character relative to surrounding sediments. Most fractures are conductive (Figs. F21, F23) with more resistive fractures identified within logging Units II and III. Fracture dips range from ~30° to 80° with no clear pattern in dip magnitude variation between logging units.

Overall orientation of fractures within the borehole is scattered. However, when fractures are divided into the four logging units (Fig. F24), distinct trends can be identified. Logging Units I and II are characterized by fractures predominantly striking northwest–southeast. In contrast, logging Units III and IV are characterized by fractures striking northeast–southwest.

In logging Unit I a second set of fractures strike northeast–southwest and dip southeastward. For the major fracture trend (northwest–southeast), fractures evenly dip toward the northeast and southwest. In logging Unit II (predominant northwest–southeast trend) many fractures dip toward the northeast. Fractures in logging Unit III are moderately scattered but with the largest subset dipping toward the northwest (trending northeast–southwest). Finally, fractures are more difficult to identify in logging Unit IV because of the high background conductivity of the borehole. For those fractures that have been identified, the predominant trend is closer to west-southwest–east-northeast and the majority dip toward the north-northwest.

Borehole breakouts

Borehole breakouts occur from 188 to 729 m LSF but are not readily discernible at greater depths. The mean azimuth of the breakouts is 060° (Fig. **F25A**) with some variation but no clear trend with depth (Fig. **F25B**). The overall mean width of breakouts is 44° (Fig. **F25C**). The weighted average of breakout widths decreases downhole, although there is considerable scatter locally to larger widths (Fig. **F25D**).

Interpretations

Bedding

Overall the bedding dip orientations below 428 m LSF are consistent with north-northwestward directed shortening, which could be caused by the plate convergence. The generally westward dips above 198 m LSF may reflect a rotation by gravitational slumping caused by a locally steep southwestward component of the topographic slope (Fig. **F26**). The westward dips above 198 m LSF could therefore be explained by a northwestward tilt caused by plate convergence with a superimposed southwestward tilt caused by gravitational slumping.

Correlations of conductive fractures with seismically inferred faults

Although the borehole images do not show clear-cut fracture zones, some conductive fractures may correlate with seismically inferred faults (Fig. **F27**). For example, in the zone of subsidiary thrust faulting between 200 and 600 m LSF conductive fractures occur at 360 and 381 m LSF that are close to the seismically inferred thrust faults. Moreover, a well-developed conductive fracture zone and a fold occurs at 657 m LSF (Fig. **F23**) that may correlate with the main frontal thrust below the zone of subsidiary thrusts. Fractures recognized in the borehole images are generally moderately dipping. There may be others of shallow dip that are indistinguishable from bedding and not identified in our analysis. Notably, the fractures discussed here are not well-developed major deformation zones and their correlations with seismic data are tentative and will be tested by coring.

Logging Unit II includes four highly conductive intervals, probably sand beds. The sharp bases of the beds occur at 223, 244.5, 305, and 335 m LSF (Fig. **F1**). The seismic depth section (Fig. **F27**) shows thrust faults between some of these distinctive beds, suggesting displacement and potential repetition. The borehole images do not show obvious major faults or fracture zones separating these beds. However, as mentioned above, our detection of faults and fractures is biased toward those that are more steeply dipping. The hypothesis that these beds are repeated by thrust faulting can be tested by coring and associated dating.

Fractures

Although fracture orientations are not strongly clustered, a significant shift occurs below 428 m LSF. Northwest–southeast striking fractures in logging Units I and II (above 428 m LSF) may be related to the southwest component of slope. That is, the southwest and northeast dips could represent a conjugate fracture system related to gravitational failure along the southwest facing slope. Overall fracture orientation below 428 m LSF is consistent with northwestward directed shortening and breakout orientations. Both fractures and bedding show orientations at shallow depths that may reflect gravitational processes, whereas deeper fractures and bedding can be better explained by tectonic processes.

In comparison to IODP Sites C0001 and C0004 upslope, there are no distinct highly deformed zones or concentrations of fractures at Site C0006. Deformation at this frontal thrust location appears to be in a less evolved state than sites farther landward in the accretionary prism. Although Site C0006 shows some discrete conductive fractures that arguably correlate with seismically inferred faults, localization and intensity of structural features are significantly less than those found at Site 808 (a similar frontal thrust location) along the Muroto transect of the Nankai Trough (Ienaga et al., 2006; McNeill et al., 2004). This apparent greater intensity of strain at Site 808 relative to Site C0006 may reflect the thinner incoming sedimentary sequence at Site 808 (about half as thick as those formed at Site C0006) with approximately equivalent convergence rate or may potentially reflect different sediment properties and consequently differing style of deformation.

Borehole breakouts

The decrease in mean breakout width with depth may indicate increasing rock strength with depth, although considerable scatter toward higher values suggests weak intervals persist. The lack of obvious breakouts below 729 m LSF occurs just below the transition to logging Unit IV, which is interpreted as dominated by sand. Excessive washouts in this interval may obscure the breakouts, but some sandy units uphole also show large caliper readings and do produce distinguishable breakouts. The breakouts indicate an S_{Hmax} orientation of 330°, which is generally consistent with that observed at Sites C0001 and C0004 but slightly divergent from the S_{Hmax} expected from the convergence direction of the Philippine Sea plate and Japan (Fig. **F26**).

Log-seismic correlation

Seismic reflection interpretation

The upper part of Hole C0006A penetrated a section of accreted trench strata at the prism toe. The section is cut by several northwest-dipping thrust faults that offset the sedimentary reflections. At least two reflections, shown in yellow and blue on Figure **F27,** are repeated at the borehole by thrust faults. The deepest fault, which continues to the southeast, is inferred to be the main frontal thrust between the overriding thrust sheet and the underthrusting trench sediment section. The complex pattern of reflections below the main frontal thrust is believed to represent channels within the upper part of the trench sediment section that are being overridden by the thrust sheet above.

Check shot survey data

Check shot data were acquired at 44 depths in Hole C0006B. Two stations were unusable because of excessive noise levels and two others were above the seafloor, but the remaining 40 stations yielded excellent quality waveforms (Fig. **F28**). These data sample depths from the seafloor to 863.09 m LSF. Approximately 15 air gun array shots were fired at each station during LWD drilling, and eight shots were fired at each station during the pipe trip out of the hole. We note that before tripping out of the hole, only one 9.5 m joint was removed, rather than the planned two, so a nonuniform station spacing resulted.

Noisy traces and traces with poor first arrival waveforms were deleted. The remaining traces were filtered (trapezoidal, zero phase, and 30-40-150-200 Hz band-pass) and stacked to produce the traces shown in Figure **F28.** The first arrival wavelet is unambiguous on all traces.

The first arrival time was picked manually to yield a correlation between seismic traveltime and depth (Table **T8**). Raw interval and average velocities were determined for each interval. We applied a damped least-squares inversion to the observed depth-time data (Lizarralde and Swift, 1999). This inversion determines a smooth velocity-depth curve by varying the arrival times by amounts that are within their uncertainty. We estimated the uncertainty of the arrivals to be ~0.3 ms. We used an inversion damping coefficient of 0.5 because it produced a χ^2 value consistent with the optimal balance between overfitting and underfitting the data. The improvement in estimated interval velocities, indicated by the smoothness of the curve and the general downward increase of velocity (Fig. **F29**), is dramatic. The accompanying changes in arrival times are very small. We used smoothed arrival picks and tool depths as the check shot curve, which we then used for correcting the seismic depth section through the drill site (Fig. **F27**).

We were not able to construct a meaningful vertical seismic profile (VSP) using these data. We tried a number of filtering and gain combinations but could not identify coherent upward-traveling reflections. We attribute this to noise from the banging of the drill pipe in the current and other sources of downhole noise.

Overall log unit correlation

To visualize the correlation of log and seismic reflection data at this site, we present a series of figures (Figs. **F28, F29, F30, F31, F32, F33, F34**) in which we have superimposed logs over a portion of the check shot–corrected prestack depth-migrated seismic reflection profile. Logging units do not correlate well with the seismic reflection data, probably because the section is strongly faulted (Fig. **F30**). Several features in the LWD logs do, however, correlate with features in the seismic data. For example, the sandy layers (low gamma ray values and low resistivity) at ~220, 240, 300, and 335 m LSF correlate with strong reflections and appear to be parts of the same unit that have been repeated as a result of thrusting (Figs. **F27, F31, F32, F33**). Several seismically defined thrust faults also correlate with features in the resistivity images, such as the conductive fractures at 360 and 381 m LSF (see **"Structural geology and geomechanics"**). The main frontal thrust correlates with a dramatic increase in hole size (Fig. **F34**) and may correlate with a fracture at 657 m LSF (Fig. **F29**).

Discussion and synthesis

Site C0006 is located at the toe of the entire accretionary prism near the trench floor, and drilling targeted the main frontal thrust at ~700 mbsf, as well as uplifted and complexly faulted sediments in the thrust sheet and less deformed trench fill in the footwall of the main frontal thrust. Hole C0006B was drilled with a full LWD tool string except for nuclear tools to TD (885.5 m LSF). Because the water depth was beyond the ROV limit of 3000 m, holes were drilled without ROV monitoring. Drilling was smooth; however, the loss of MWD communication effectively eliminated sonic data acquisition from 274 to 885.5 m LSF. Drilling at this site set the record for the deepest water depth (3871.5 m) drilled by the *Chikyu*.

Four logging units were defined based on differing trends and the character of LWD log responses. Logging Unit I (0–197.8 m LSF) is interpreted as sandy and muddy deposits. Logging Unit II (197.8–428.3 m LSF) is interpreted as mud with occasional thick (~5 m) sand layers. Logging Unit III (428.3–711.5 m LSF) is defined as alternating beds of mud and sand and is divided into two subunits. The base of logging Unit II is interpreted as a possible fault zone as well as a distinct lithologic boundary. Logging Unit III (711.5 m LSF to TD) is characterized by low gamma ray values and low resistivity and is interpreted as sandy deposits. Logging Unit IV has the lowest gamma ray values and is interpreted as underthrust, coarse, trench-fill sediments.

Faults within the thrust sheet

Within logging Unit II at Site C0006, sediment layers are cut by several northwest-dipping thrust faults that offset sedimentary reflections. The resistivity image and other properties at this site, however, show only moderate fracturing with no obvious major faults or fracture zones separating these layers.

Logging Unit II includes four highly conductive intervals, probably ~5 m thick sand beds. The sharp bases of these beds occur at 223, 244.5, 305, and 335 m LSF. The seismic depth section (Figs. **F27**, **F30**) shows faults between some of these distinctive beds, suggesting thrust displacement and potential repetition. The hypothesis that these beds are repeated by thrust faulting was tested by coring and associated dating during Expedition 316.

Main frontal thrust

The gamma ray baseline gradually increases with depth throughout logging Units I–III. Within logging Unit IV below 711 m LSF, the gamma ray value suddenly decreases from ~90 gAPI at the bottom of Unit III to 20–50 gAPI in Unit IV. Lower resistivity and larger borehole diameter accompany this low gamma ray trend, indicating that Unit IV is dominated by unconsolidated sand. From lithologic interpretation, we interpret that Unit IV corresponds to the underthrust trench-fill sediments and that the Unit III/IV boundary corresponds to the main frontal thrust.

Alternatively, from structural interpretation of resistivity images, a well-developed conductive fracture zone (~1 m thick) and a fold occur at 657 m LSF (Fig. **F23**) within logging Unit III, across which the resistivity abruptly decreases following a thick zone of high resistivity. Although no significant change in gamma ray response is present, this fracture zone and change in the resistivity log may correlate with the main frontal thrust below the zone of subsidiary thrusts, although we acknowledge that this feature does not appear as a major fault zone. The complex pattern of seismic reflections below the main frontal thrust may represent channels within the upper part of the trench sediment section that are being overridden by the thrust sheet.

Deformation and stress orientation near the toe of accretionary prism

Analysis of both bedding and fracture orientation at Site C0006 documents how the formation has been deformed under the local or regional stress field.

Within logging Unit I, bedding planes are west-dipping. In logging Unit II, bedding dip and orientation patterns show variability. Bedding is predominantly north-dipping in logging Units III and IV.

Fractures at Site C0006 are notable in that they are not as clustered into zones as those found at Sites C0001 or C0004, and no major deformed zones are identified, suggesting generally weaker deformation at Site C0006. Fractures mostly strike northwest–southeast in logging Units I and II (<428 m LSF), whereas fractures in Units III and IV (429–853 m LSF) strike northeast–southwest.

Overall, both fracture and bedding orientations at depths >429 m LSF are consistent with northwesterly directed shortening resulting from plate convergence. Fracture and bedding orientations at these depths are also consistent with breakout orientations. At shallower depths, fracture and bedding orientations deviate from this general orientation and probably result from combined regional tectonic and local effects (such as gravitational processes).

Borehole breakouts occur from 188 to 729 m LSF but are not readily discernible at greater depths. Taken as a whole, breakouts are more weakly developed at Site C0006 than at any of the upslope sites. Breakouts

show mean S_{Hmax} orientation of 330° with little variation downhole, consistent with that observed at Sites C0001 and C0004 but slightly divergent from the S_{Hmax} expected from the convergence direction between the Philippine Sea plate and Japan. The lack of obvious breakouts below 729 m LSF occurs just below the transition to logging Unit IV, which is dominated by sand. Excessive washouts in this interval may have obscured the breakout signal.

In logging Unit III (429– 711 m LSF), fracture and bedding orientation is in agreement with the S_{Hmax} direction calculated from breakouts. Within logging Units I and II, however, fracture and bedding orientations are not what is predicted by S_{Hmax} orientation. The reason for this is unclear, but detailed postcruise research (integrating log, core, and seismic data) may help to resolve this issue.

References

Ashi, J., Kuramoto, S., Morita, S., Tsunogai, U., Goto, S., Kojima, S., Okamoto, T., Ishimura, T., Ijiri, A., Toki, T., Kudo, S., Asai, S., and Utsumi, M., 2002. Structure and cold seep of the Nankai accretionary prism off Kumano—outline of the off Kumano survey during YK01-04 Leg 2 cruise. *JAMSTEC J. Deep Sea Res.,* 20:1–8.

Heki, K., 2007. Secular, transient and seasonal crustal movements in Japan from a dense GPS array: implication for plate dynamics in convergent boundaries. *In* Dixon, T., and Moore, C. (Eds.), *The Seismogenic Zone of Subduction Thrust Faults:* New York (Columbia Univ. Press), 512–539.

Ienaga, M., McNeill, L.C., Mikada, H., Saito, S., Goldberg, D., and Moore, J.C., 2006. Borehole image analysis of the Nankai accretionary wedge, ODP Leg 196: structural and stress studies. *Tectonophysics,* 426(1–2):207–220. **doi:10.1016/j.tecto.2006.02.018**

Kinoshita, M., Goto, S., Hamamoto, H., and Yamano, M., 2003. Heat flow distribution and thermal regime across the Nankai accretionary complex. *Eos, Trans. Am. Geophys. Union,* 84(46)(Suppl.):T42C-06. (Abstract)

Lizarralde, D., and Swift, S., 1999. Smooth inversion of VSP traveltime data. *Geophysics,* 64(3):659–661. **doi:10.1190/1.1444574**

McNeill, L.C., Ienaga, M., Tobin, H., Saito, S., Goldberg, D., Moore, J.C., and Mikada, H., 2004. Deformation and in situ stress in the Nankai accretionary prism from resistivity-at-bit images, ODP Leg 196. *Geophys. Res. Lett.,* 31(2):L02602. **doi:10.1029/2003GL018799**

Miyazaki, S., and Heki, K., 2001. Crustal velocity field of southwest Japan: subduction and arc-arc collision. *J. Geophys. Res.,* 106(B3):4305–4326. **doi:10.1029/2000JB900312**

Moore, G.F., Bangs, N.L., Taira, A., Kuramoto, S., Pangborn, E., and Tobin, H.J., 2007. Three-dimensional splay fault geometry and implications for tsunami generation. *Science,* 318(5853):1128–1131. **doi:10.1126/science.1147195**

Seno, T., Stein, S., and Gripp, A.E., 1993. A model for the motion of the Philippine Sea plate consistent with NUVEL-1 and geological data. *J. Geophys. Res.,* 98(B10):17941–17948. **doi:10.1029/93JB00782**

Publication:11 March 2009
MS 314315316-118

Figure F1. Summary log diagram, Site C0006. LSF = LWD depth below seafloor. VE = vertical exaggeration. Black tadpoles = bedding, red tadpoles = fracture, tadpole line = dip direction of plane.

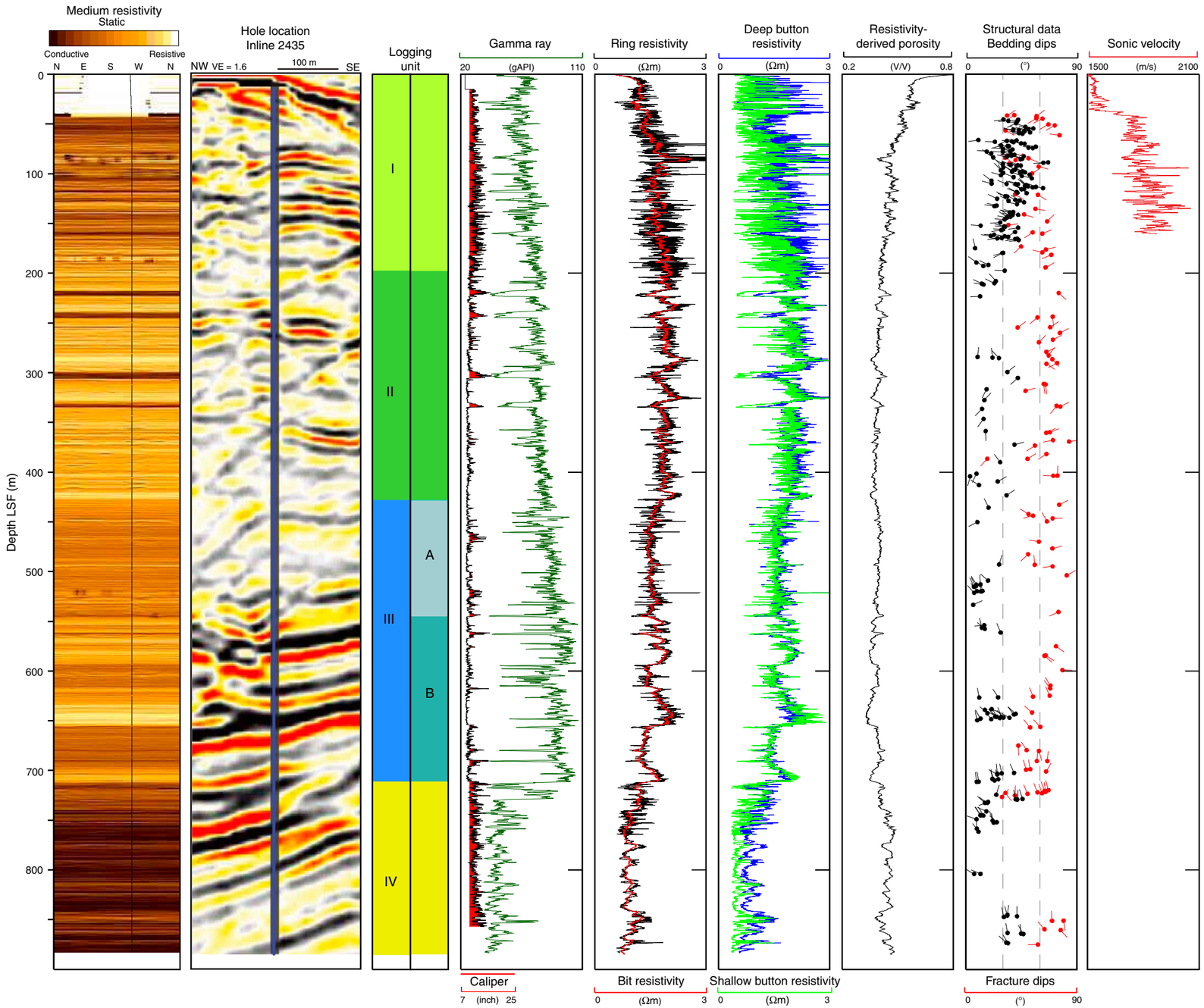

Figure F2. Inline 2435 3-D seismic profile crossing Site C0006 (Moore et al., 2007). VE = vertical exaggeration.

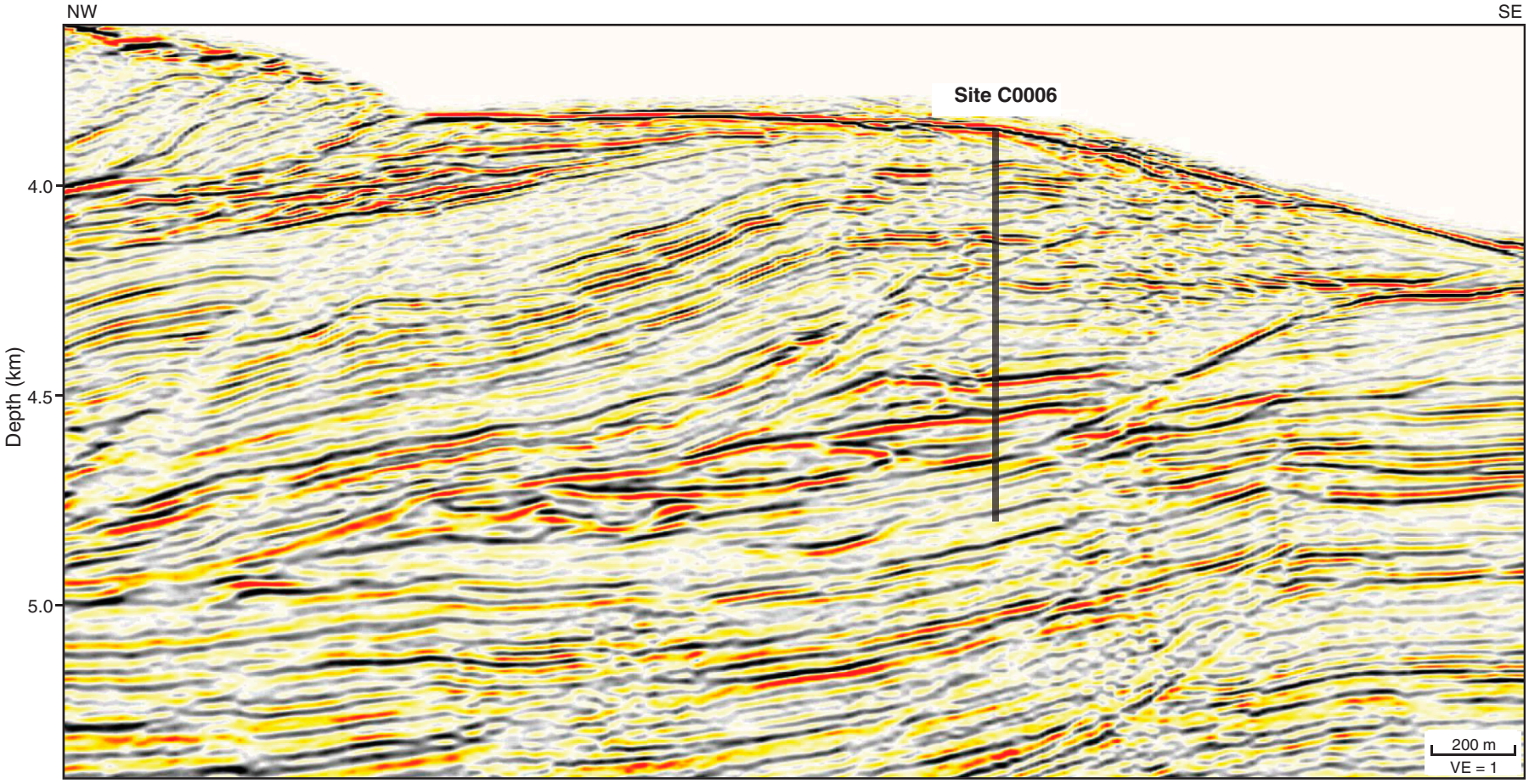

Figure F3. Drilling parameters and gamma ray log plotted vs. time for MWD-APWD operations, Hole C0006A. GR_RAB = MWD tool real-time gamma ray log, ATMP = annular temperature, ECD = equivalent circulating density, APRS = average annular pressure, TRPM = MWD turbine rotation speed (off = <1500 or >4500 rpm, on = 1500–4500 rpm), CRPM = collar rotation, SWOB = surface weight on bit, HKLD = hook load, SPPA = standpipe pressure, ROP = rate of penetration, ROP_5ft = 5 ft averaged ROP, LSF = LWD depth below seafloor, DRF = drillers depth below rig floor.

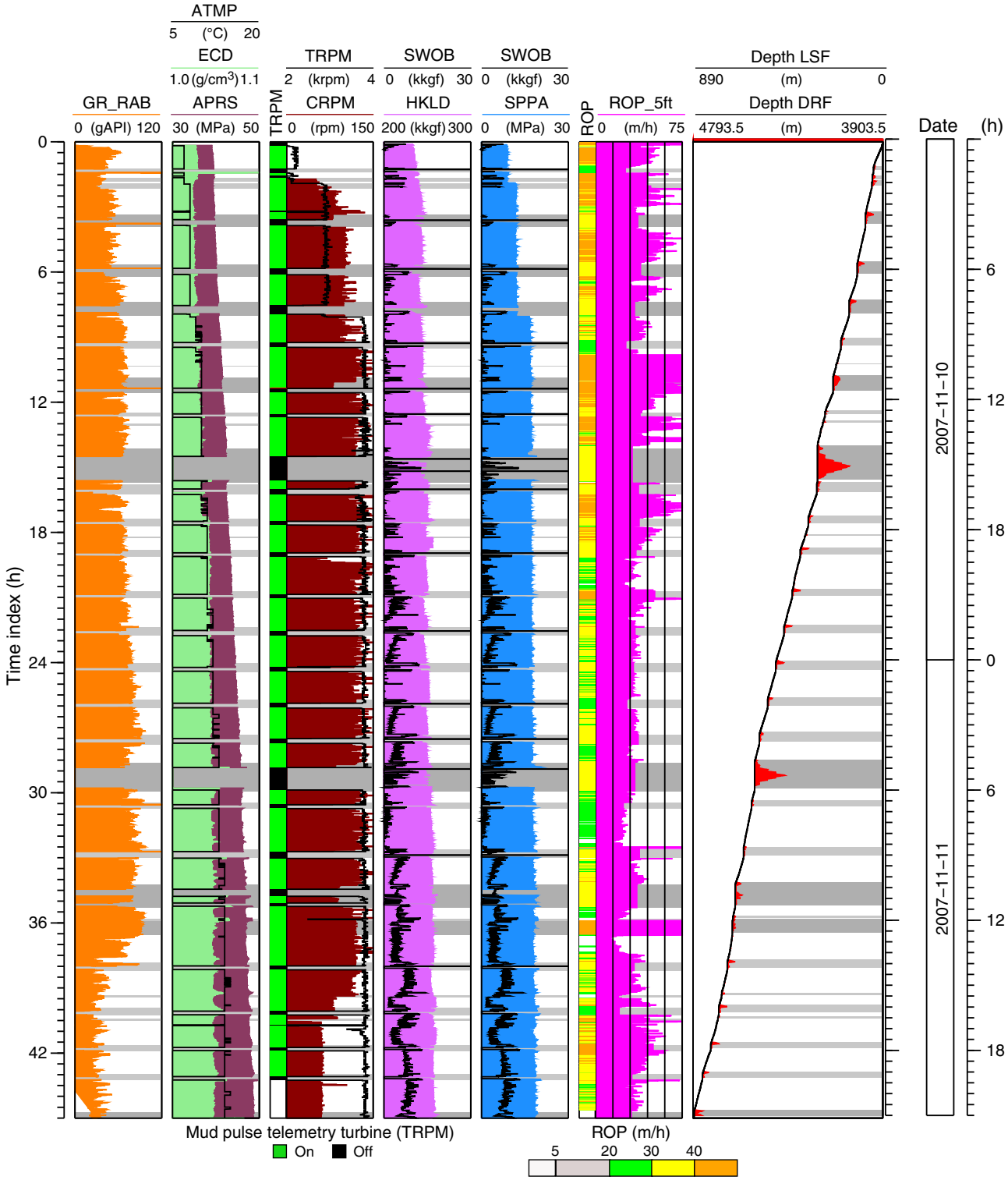

Figure F4. Drilling parameters and gamma ray log plotted vs. time for LWD-MWD-APWD operations, Hole C0006B. GR_RAB = MWD tool real-time gamma ray log, ATMP = annular temperature, ECD = equivalent circulating density, APRS = average annular pressure, TRPM = MWD turbine rotation speed (off = <1500 or >4500 rpm, on = 1500–4500 rpm), CRPM = collar rotation, SWOB = surface weight on bit, HKLD = hook load, SPPA = standpipe pressure, ROP = rate of penetration, ROP_5ft = 5 ft averaged ROP, LSF = LWD depth below seafloor, DRF = drillers depth below rig floor. Note loss of real-time communication with LWD tools at 1800 h on 13 November 2007 (345.2 m LSF).

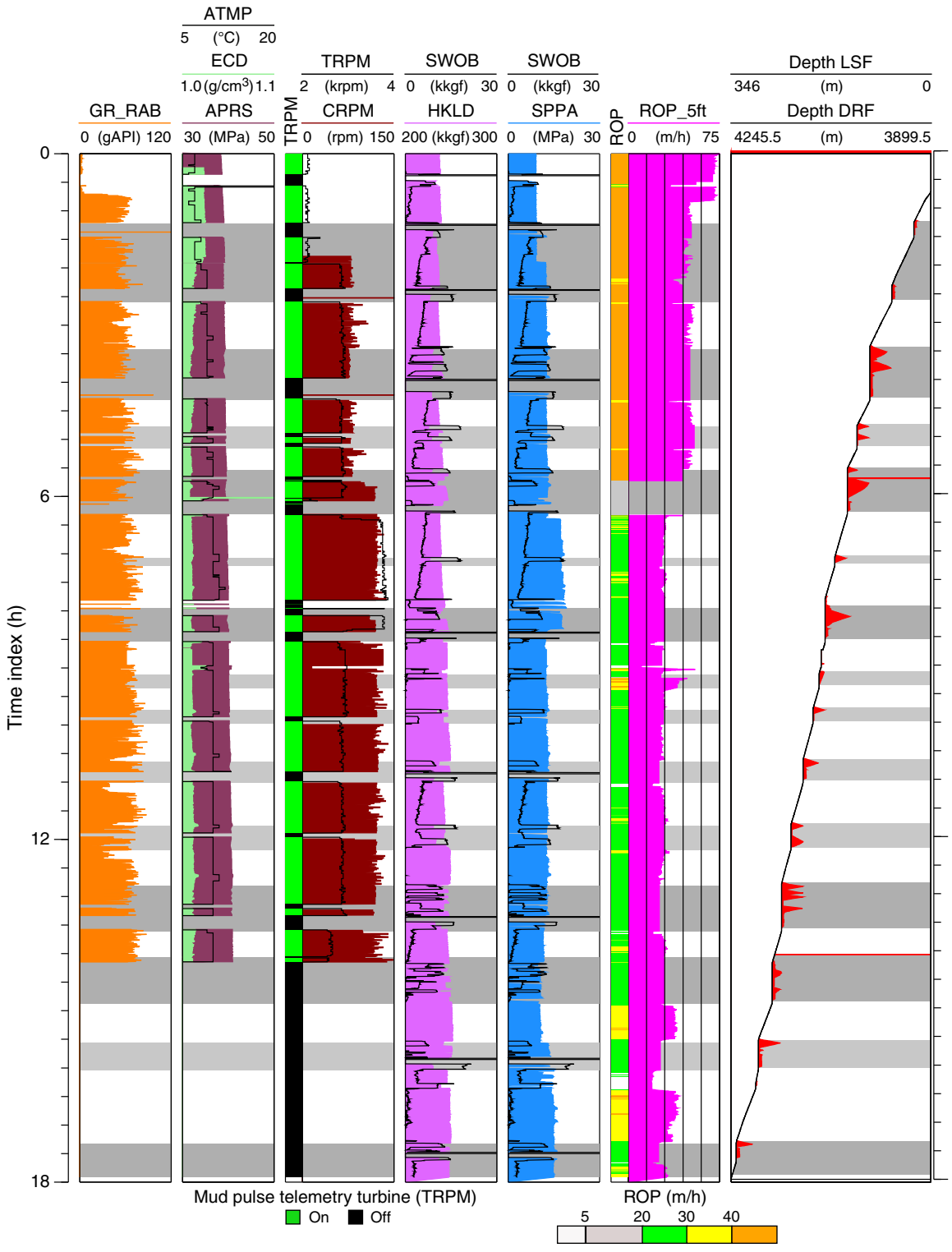

Figure F5. Mudline identification using MWD tool real-time gamma ray log, Hole C0006A. DRF = drillers depth below rig floor, LSF = LWD depth below seafloor.

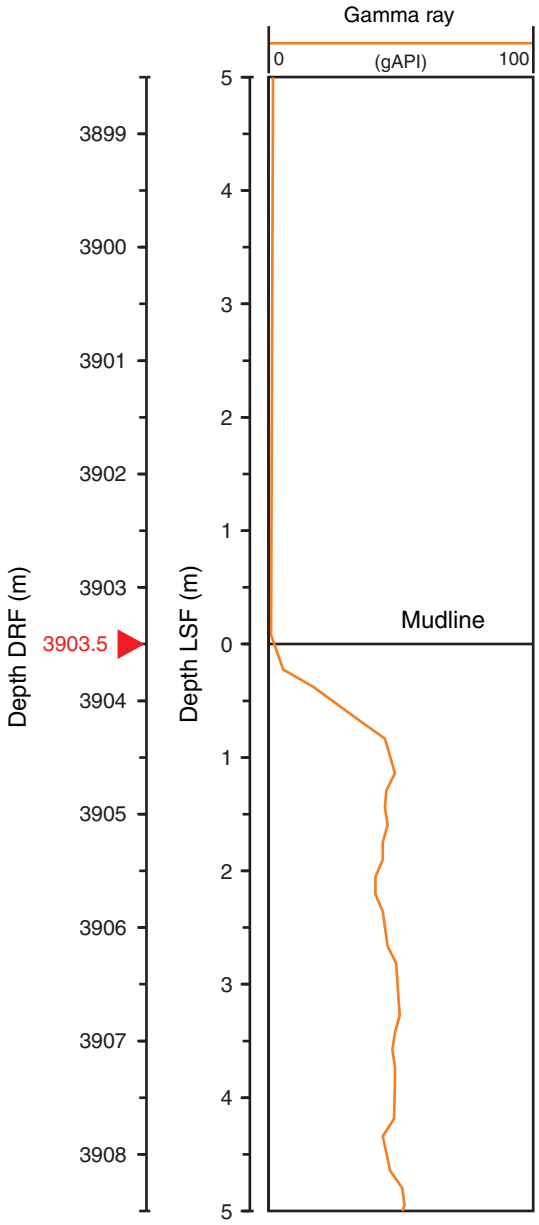

Figure F6. Control logs, Hole C0006A. LSF = LWD depth below seafloor, ROP = rate of penetration, SWOB = surface weight on bit, ROP_5ft = 5 ft averaged ROP, HKLD = hook load, SPPA = standpipe pressure, ECD = equivalent circulating density, APRS = average annular pressure, GRM1 = gamma ray (MWD).

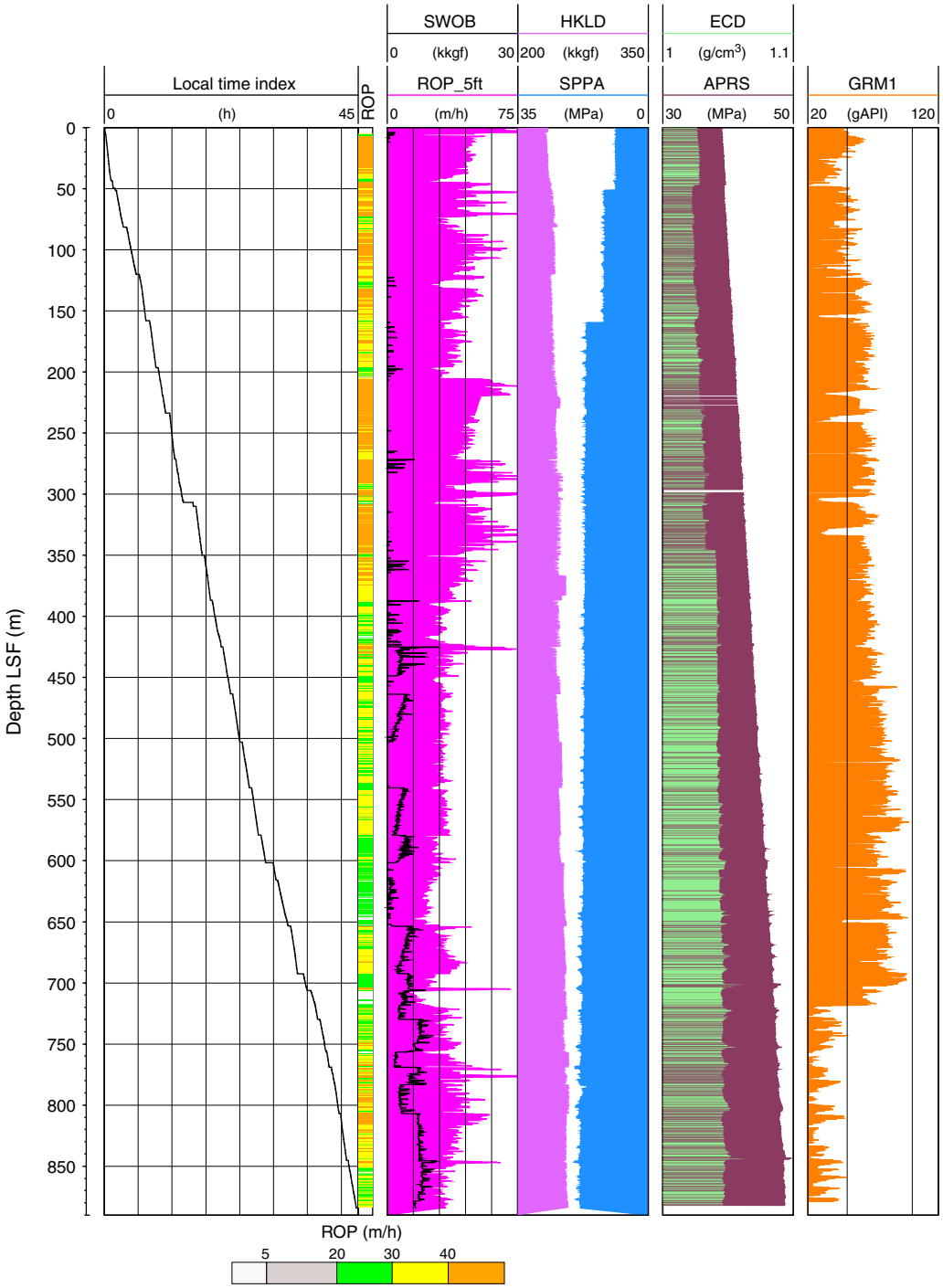

Figure F7. Plot of time-depth relationship, Hole C0006A. LSF = LWD depth below seafloor.

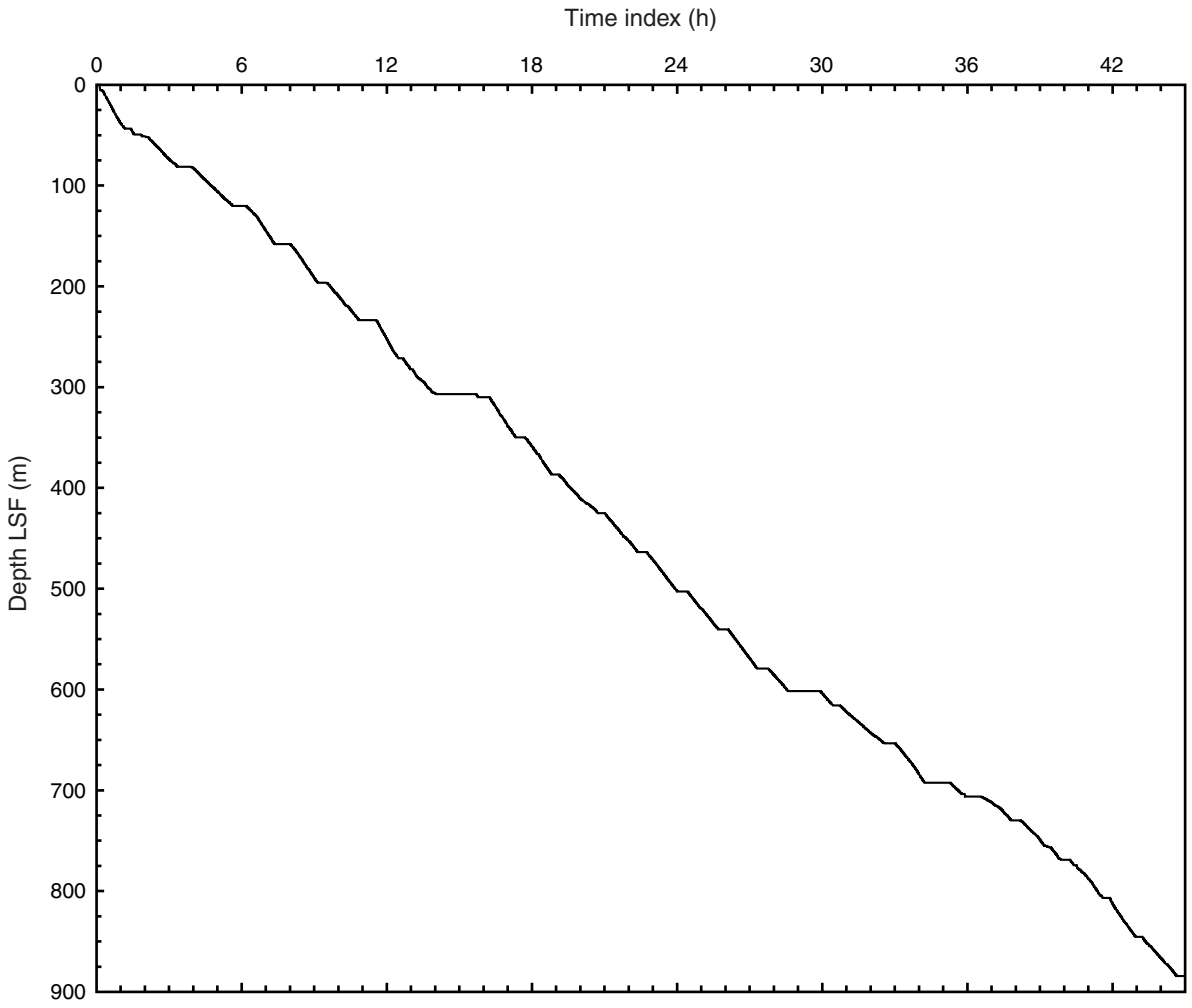

Figure F8. Control logs, Hole C0006B. LSF = LWD depth below seafloor; ROP = rate of penetration; SWOB = surface weight on bit; HKLD = hook load; SPPA = standpipe pressure; DEVI = hole deviation; ECD = equivalent circulating density; APRS = average annular pressure; CC15, CC26, CC37, and CC48 = ADN ultrasonic calipers and color coded borehole condition indicators based on ADN calipers (Cxy = C15, C26, C37, and C48); GR_RAB = Hole C0006B gamma ray log (geoVISION resistivity tool memory data) compared with Hole C0006A gamma ray log (GRM1; MWD real-time data).

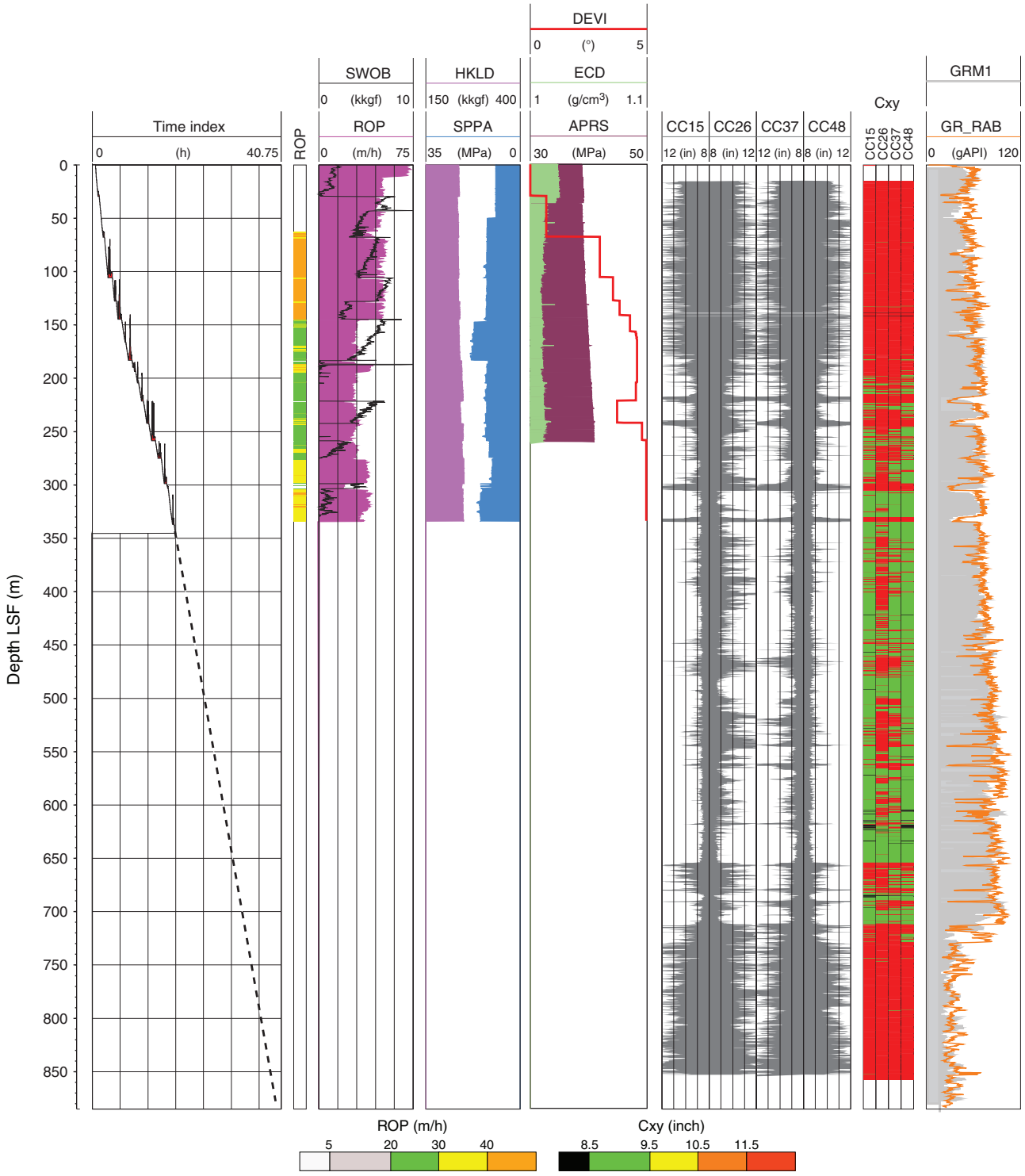

Figure F9. Mudline identification using geoVISION tool gamma ray and resistivity log (memory data, Hole C0006B. Mudline is identified by a break in gamma ray and resistivity logs at 3899.5 m drillers depth below rig floor (DRF). Note that resistivity data are plotted on a linear scale. LSF = LWD depth below seafloor.

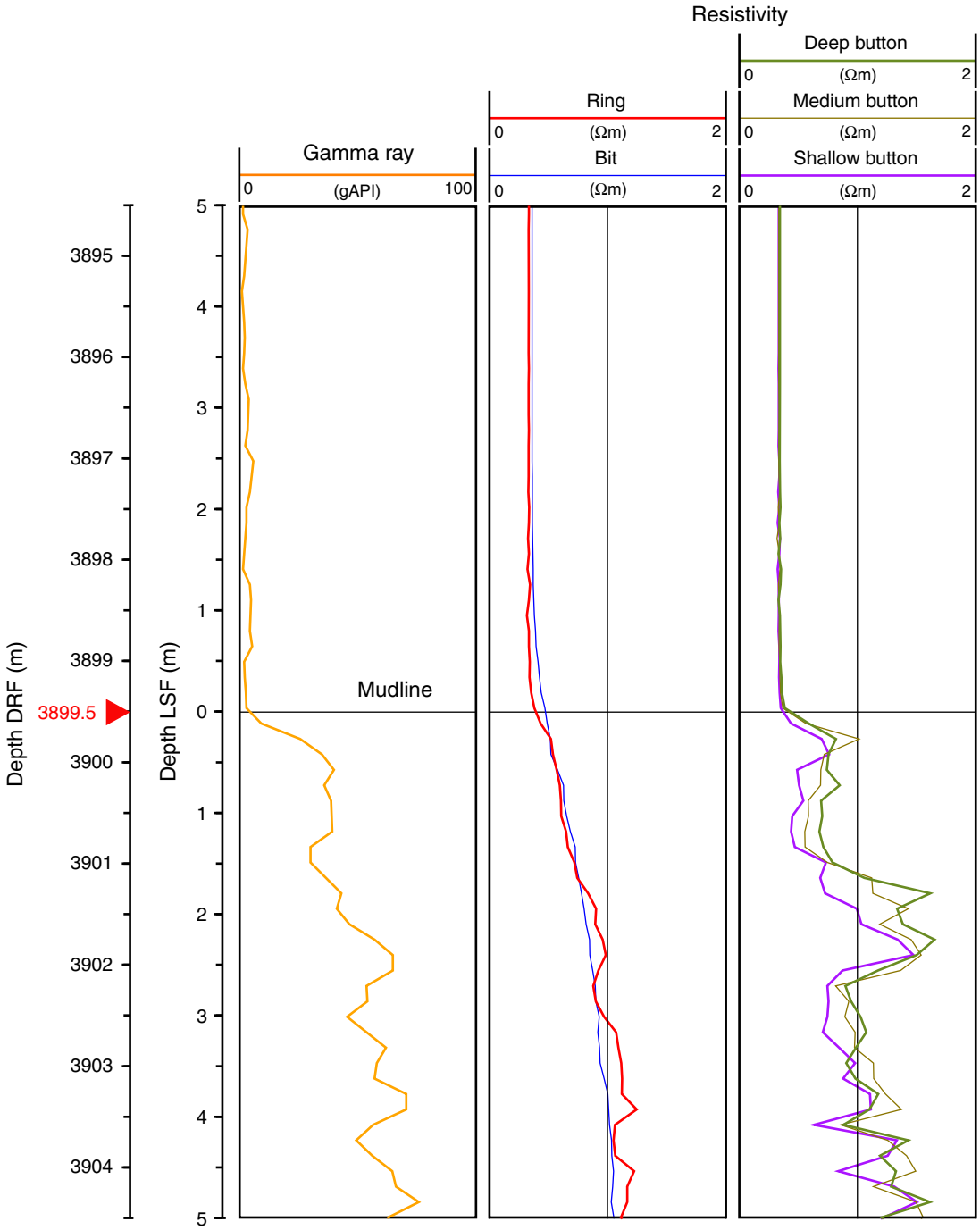

Figure F10. Geophysical logs, Hole C0006B. LSF = LWD depth below seafloor. ROP = rate of penetration; GR_RAB = gamma ray log (geoVISION resistivity [GVR] tool memory data); Cxy = ADN ultrasonic calipers C15, C26, C37, and C48; TAB_RAB_BD = time after bit of GVR deep button resistivity; TAB_RAB_BIT = time after bit of GVR bit resistivity; RES_BIT = bit resistivity; RES_RING = ring resistivity; RES_BD = deep button resistivity; RES_BM = medium button resistivity; RES_BS = shallow button resistivity; V_P = sonic compressional velocity (*P*-wave), DTCO = ΔT compressional. (**Figure shown on next page.**)

Figure F10 (continued). (Caption shown on previous page.)

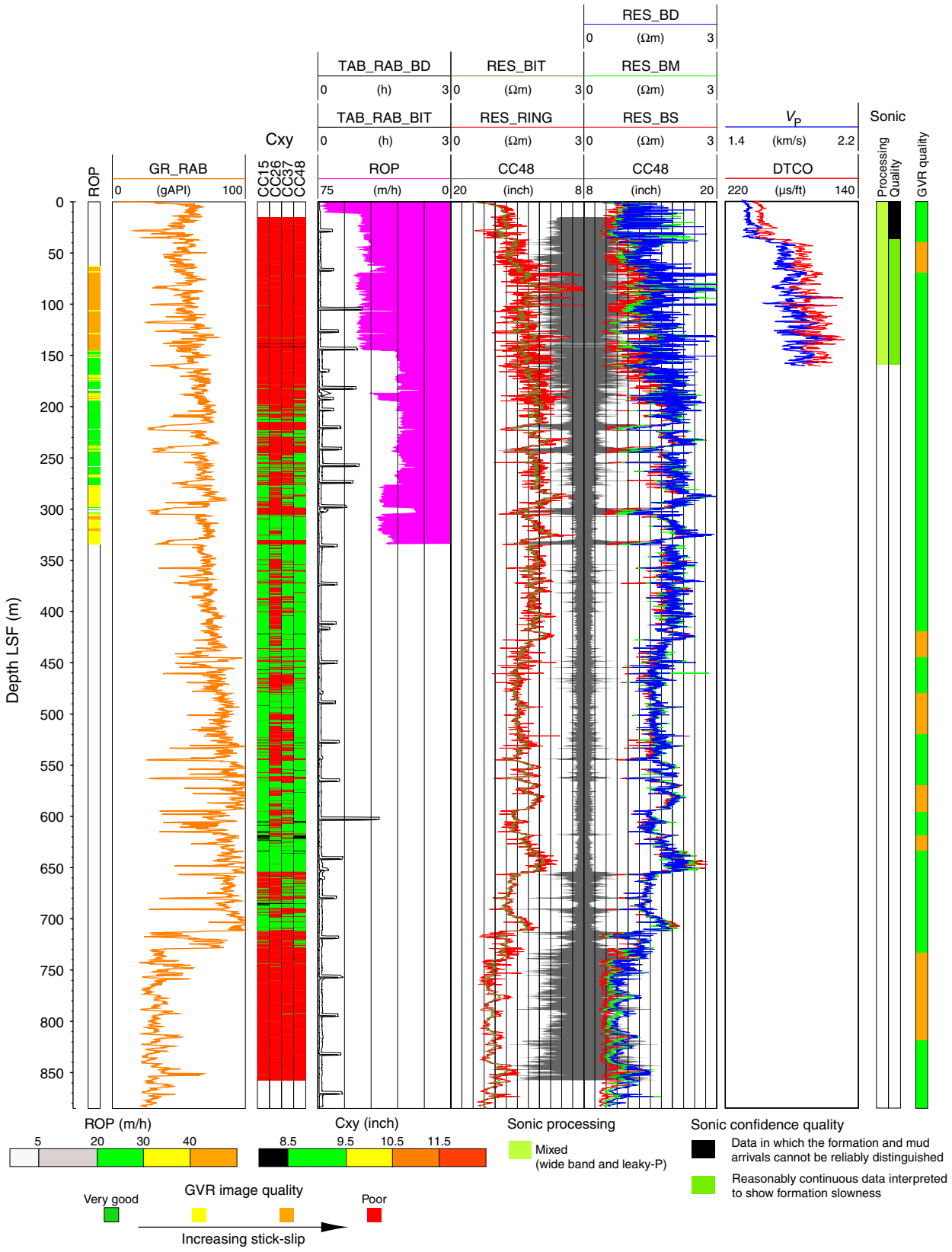

Figure F11. Plot of time-depth relationship, Hole C0006B. LSF = LWD depth below seafloor. LWD = logging while drilling, MWD = measurement while drilling.

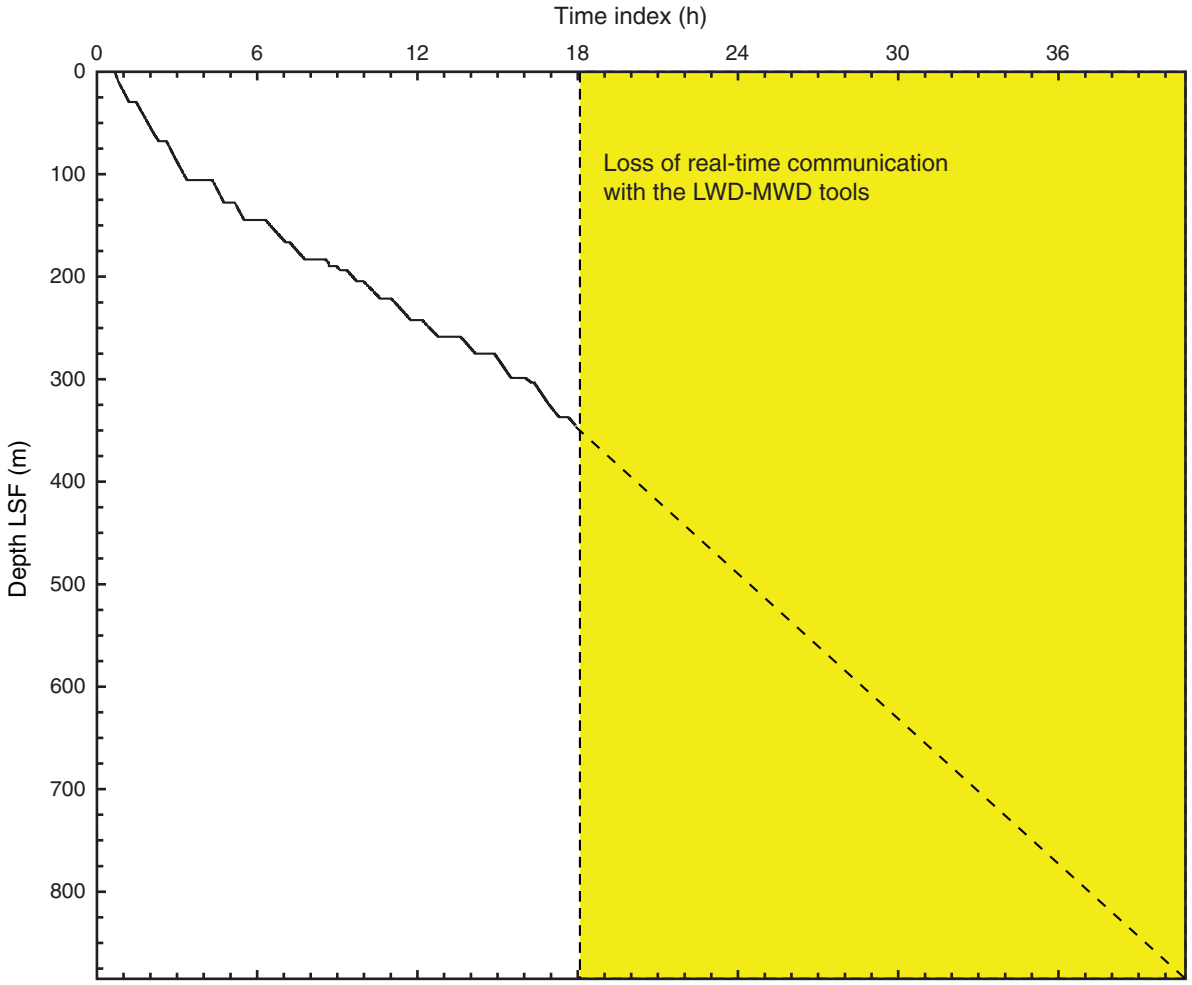

Figure F12. Statistical variation of gamma ray and ring resistivity exhibited by logging units and subunits.

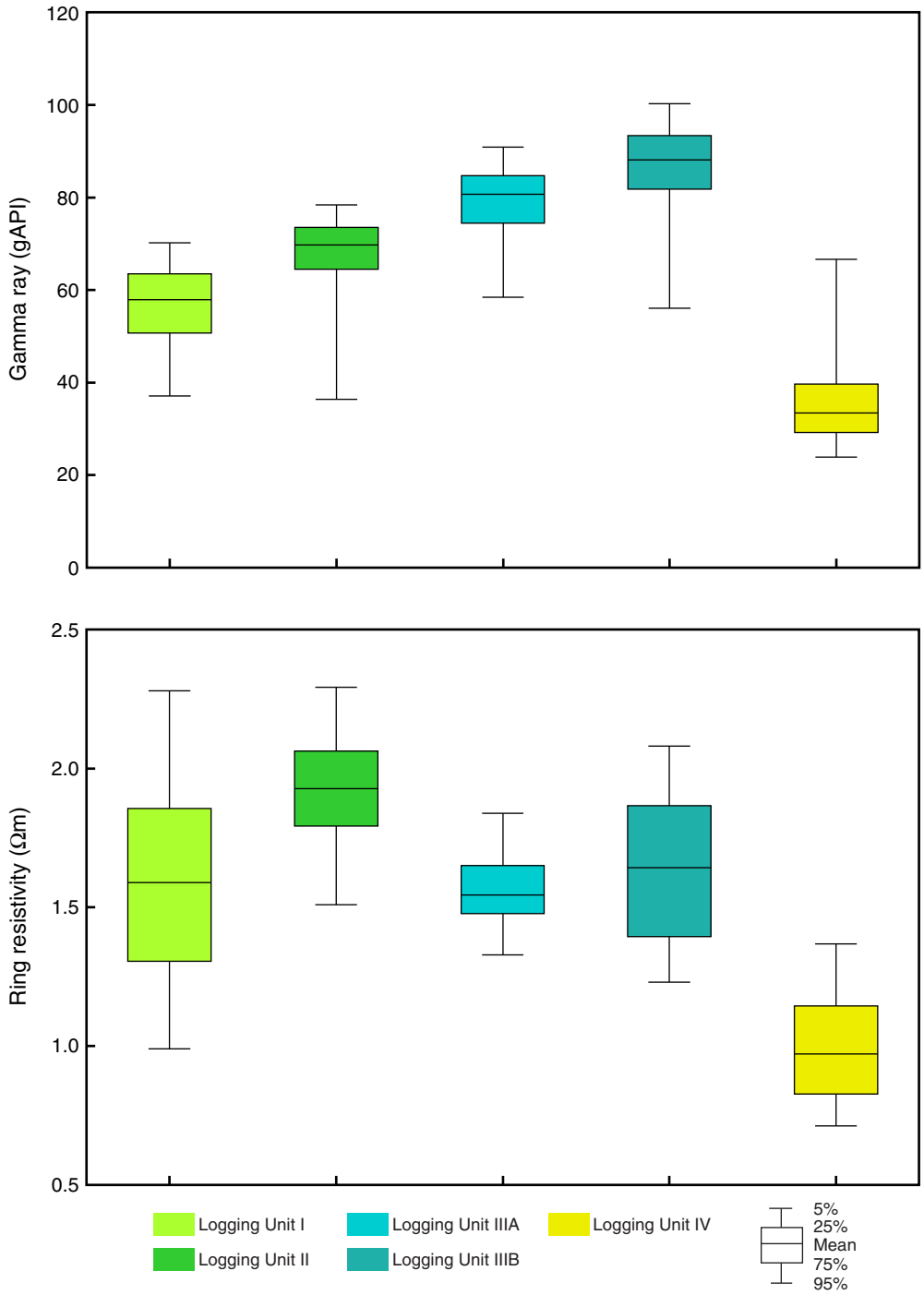

Figure F13. Plot of gamma ray vs. ring resistivity.

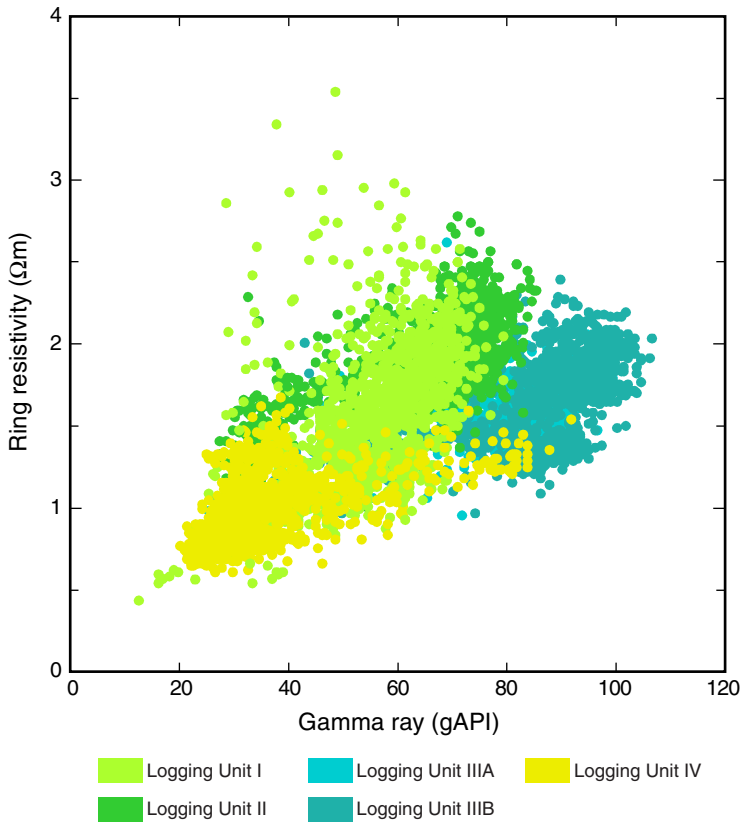

Figure F14. Summary plot of bedding dips derived from image data. LSF = LWD depth below seafloor, RAB = resistivity-at-the-bit.

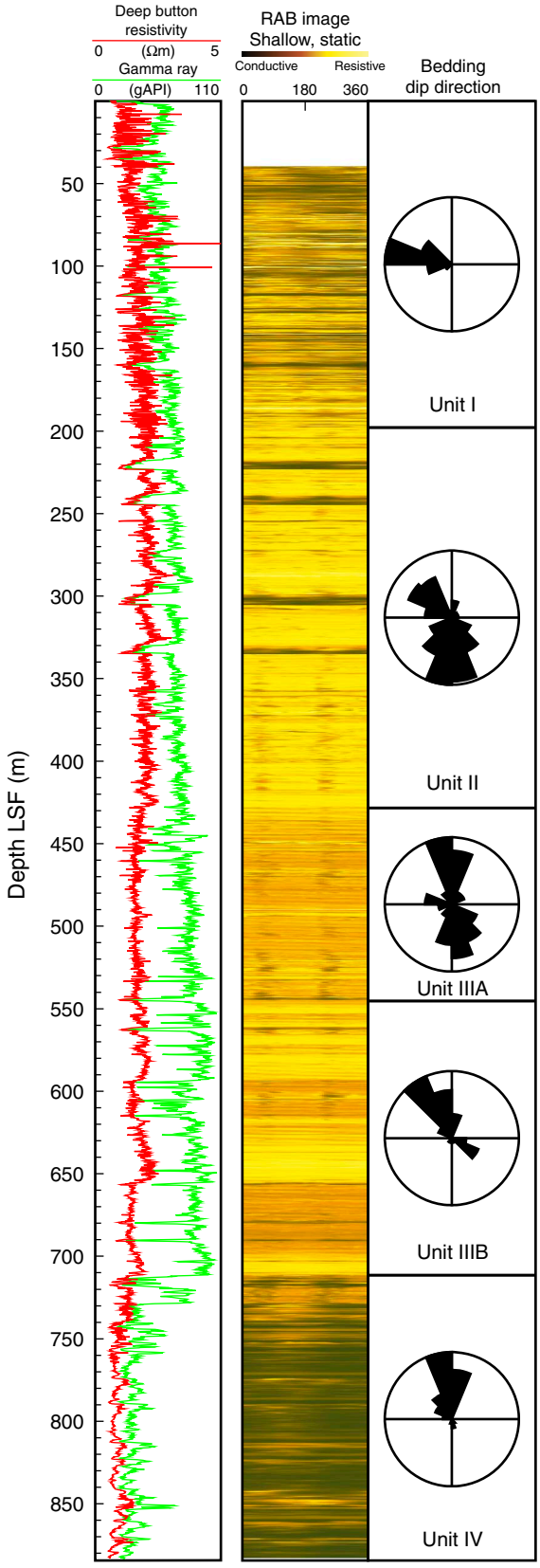

Figure F15. Logging Unit II logs. Upward-fining sequences in four sand layers are clearly imaged by resistivity-at-the-bit (RAB) images and exhibited by gamma ray (GR) and resistivity log curves. An inferred thrust fault at 254 m LWD depth below seafloor (LSF) is shown.

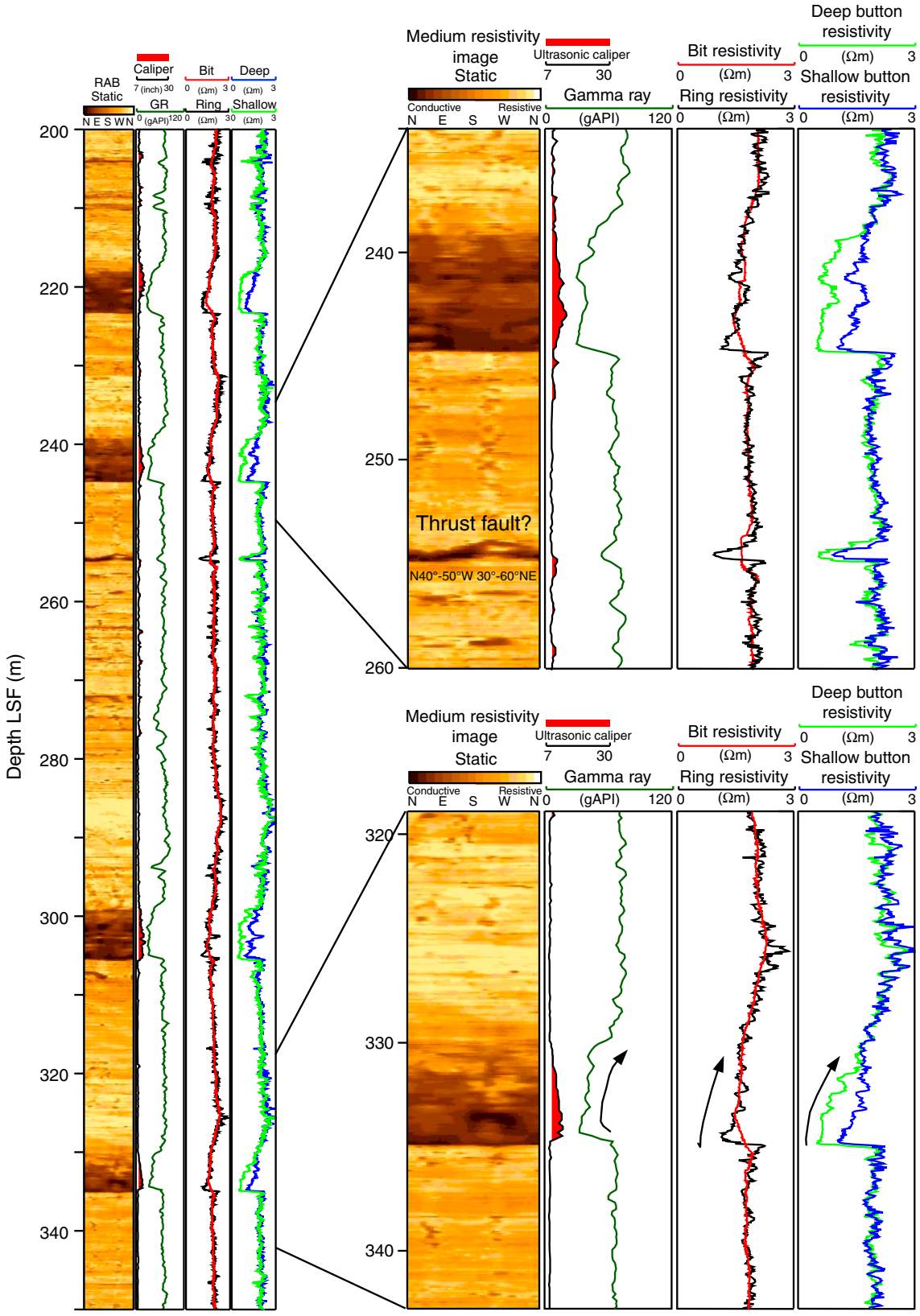

Figure F16. Ring and bit resistivity and smoothed shallow, medium, and deep button resistivity logs. Smoothing results from a moving average of the resistivity values using a 21-point window. LSF = LWD depth below seafloor.

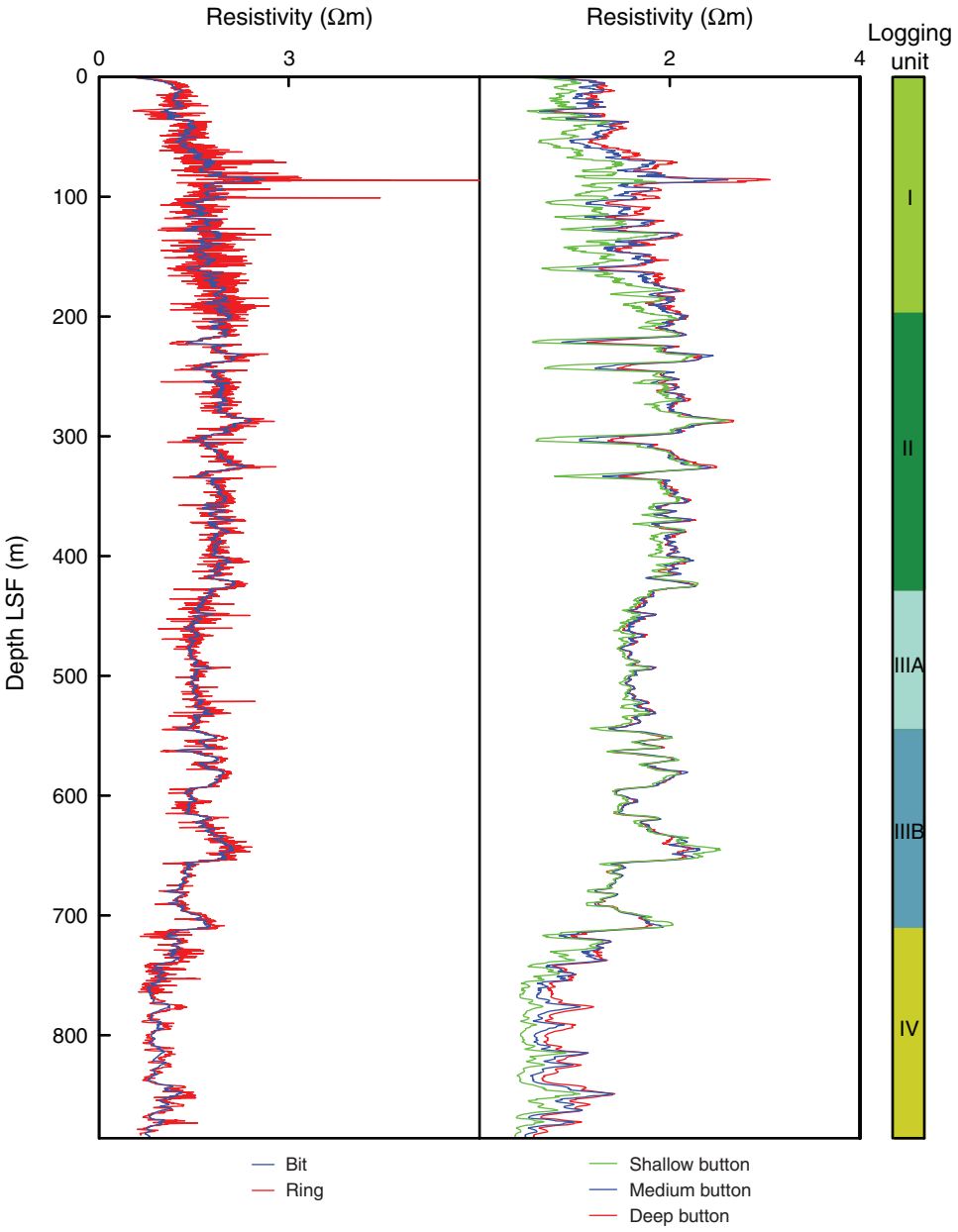

Figure F17. Plots of (**A**) bit vs. ring resistivity and (**B**) shallow vs. deep button resistivity. Black line = line of unit slope passing through origin.

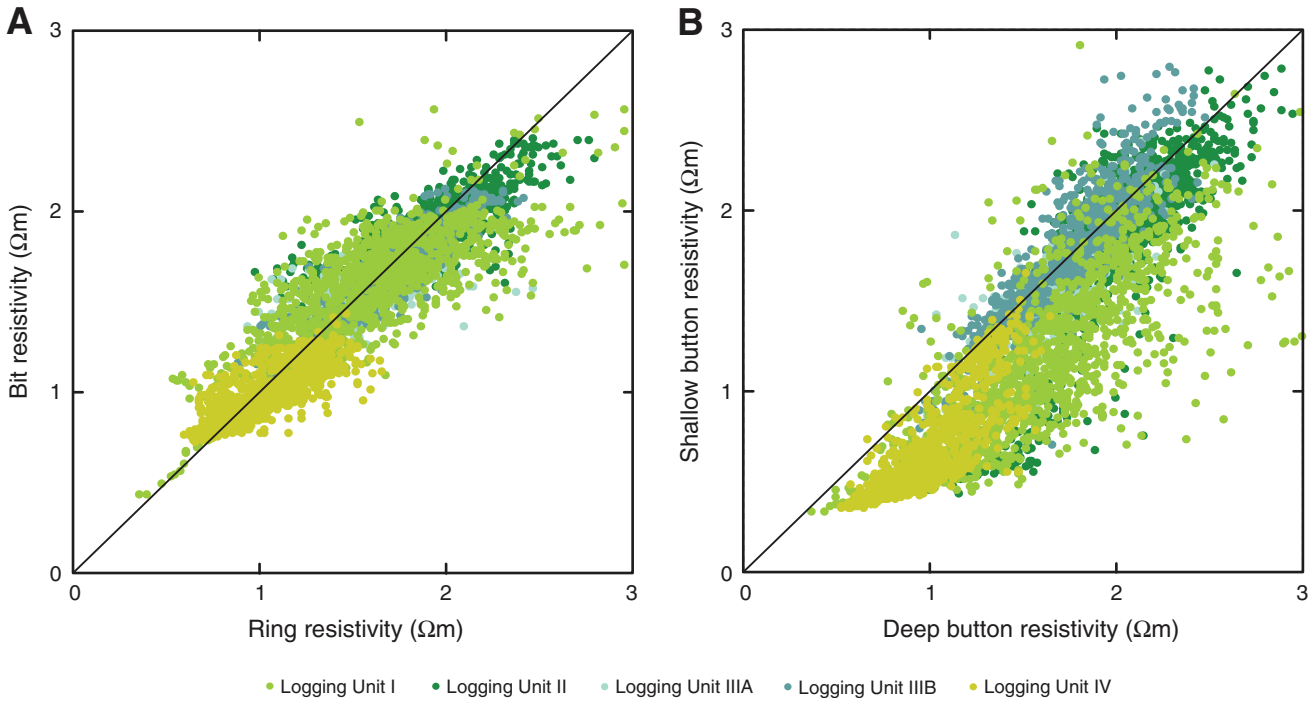

Figure F18. Bit and ring resistivity–derived porosity and density calculated from porosity using Archie's law with parameters $a = 1$ and $m = 2.4$ (see **"Physical properties"** for discussion of possible lithology dependence). LSF = LWD depth below seafloor.

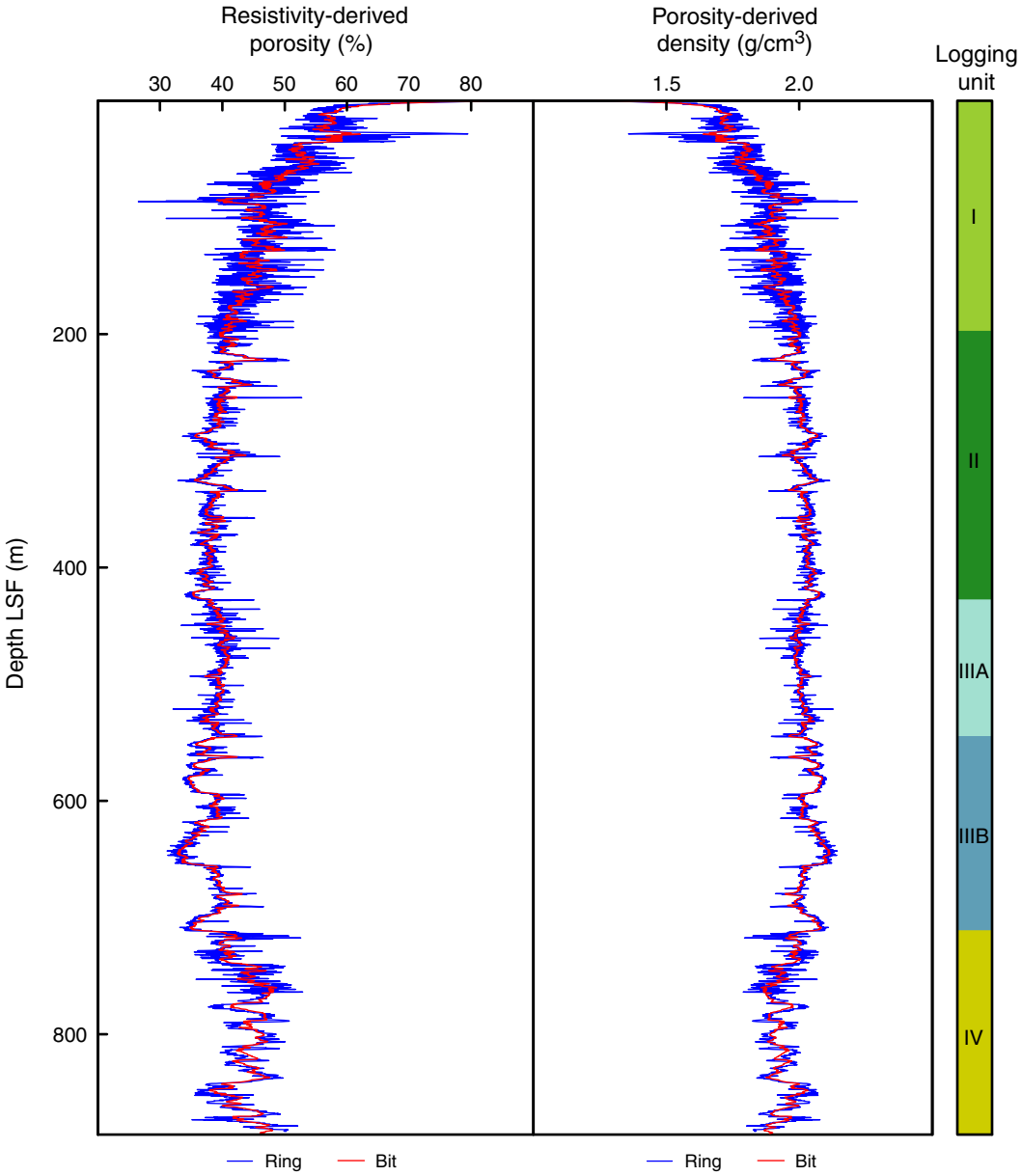

Figure F19. Comparison between sonic *P*-wave velocity and resistivity, Hole C0006A. LSF = LWD depth below seafloor.

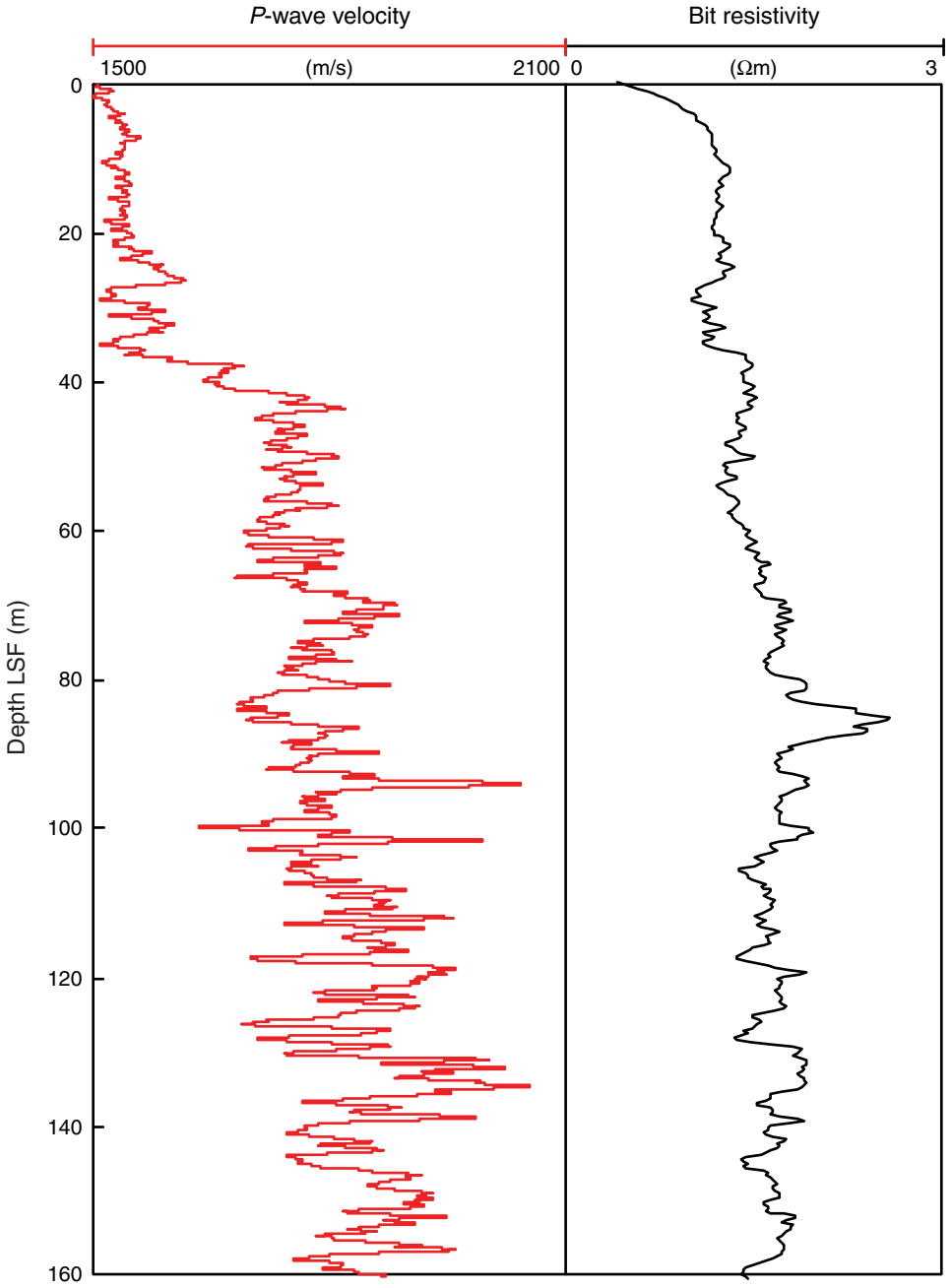

Figure F20. Plot of sonic *P*-wave velocity vs. resistivity, Hole C0006A.

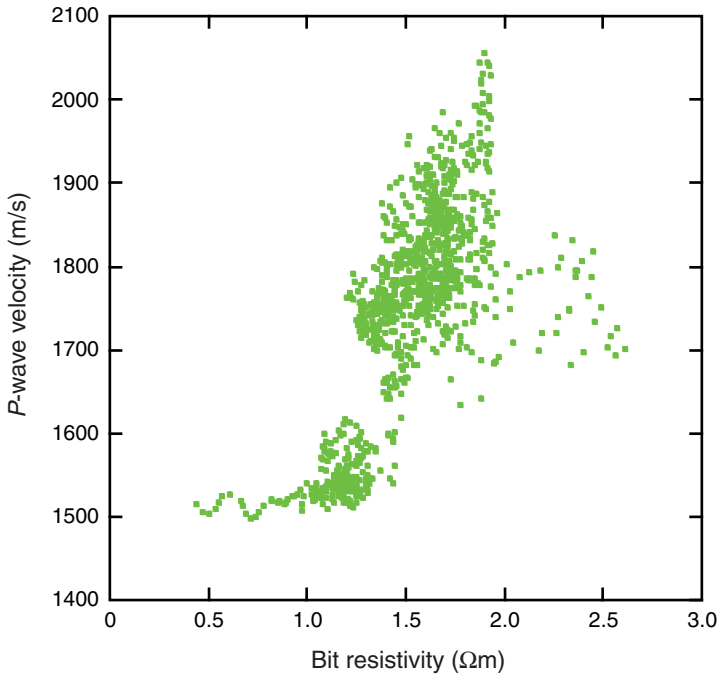

Figure F21. Vertically compressed shallow resistivity image (dynamic normalization) of borehole showing trends in bedding and fractures. Tadpole lines = dip direction of plane. LSF = LWD depth below seafloor.

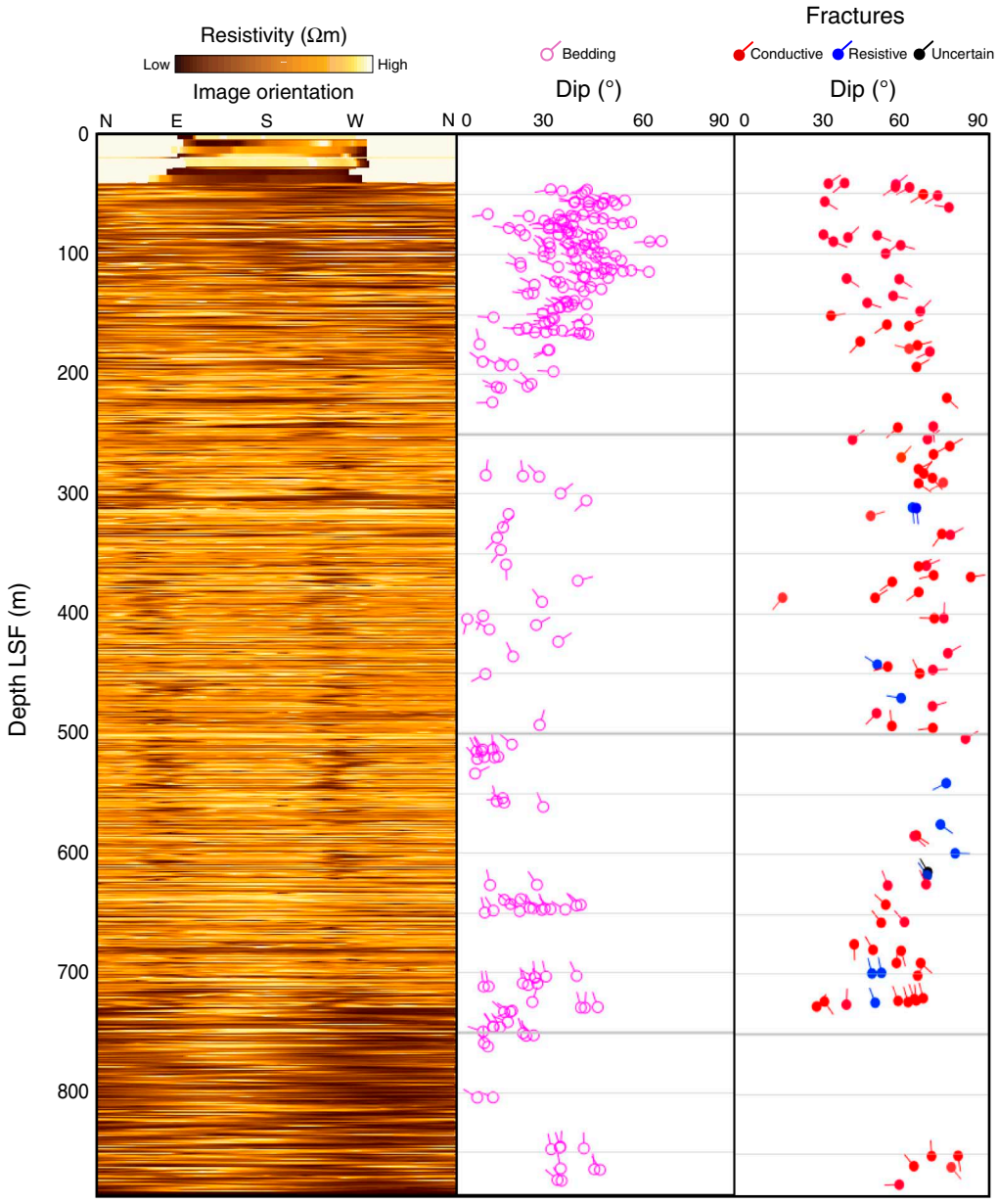

Figure F22. Bedding orientations in each logging unit. Left column = equal area lower hemisphere projections of poles to bedding, right column = rose diagrams representing azimuths (shown as dip direction –90°) preserving dip direction information. Note dominantly westerly dip of bedding in logging Unit I and northwestward dips of bedding in logging Units III and IV. LSF = LWD depth below seafloor. TD = total depth.

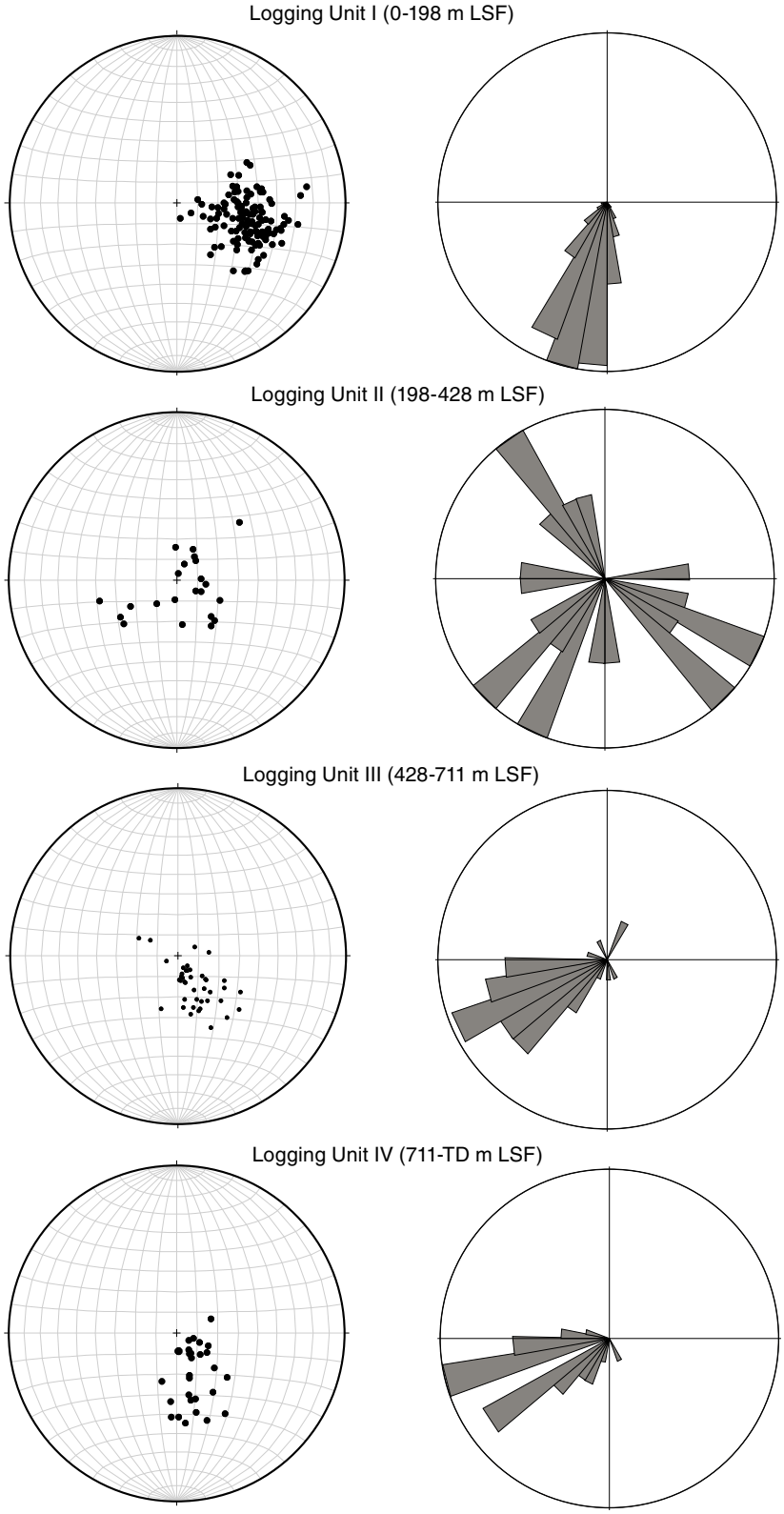

Figure F23. Uninterpreted and interpreted image of conductive fracture with an immediately overlying fold at 656–657 m LWD depth below seafloor (LSF). Conductive fracture may correlate with seismic interpretation of main frontal thrust.

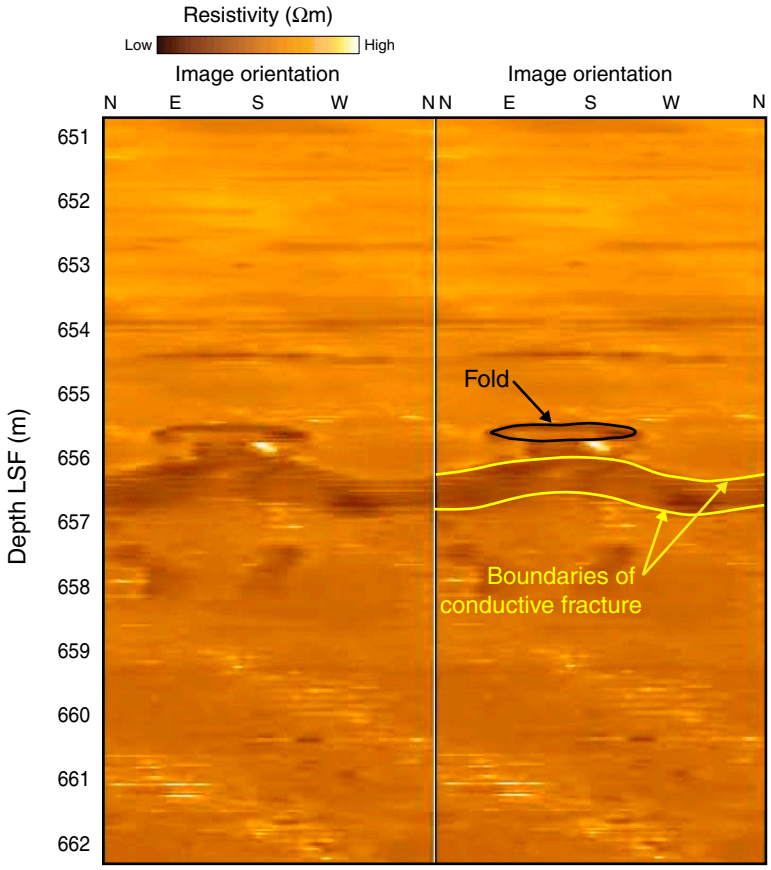

Figure F24. Fracture orientations in each logging unit. Left column = equal area lower hemisphere projections of poles to fracture planes, right column = rose diagrams showing fracture strikes (shown as dip direction –90°) preserving dip direction information. Note predominance of northwest fracture orientations in logging Units I and II in contrast to northeast–southwest orientations of logging Units III and IV. LSF = LWD depth below seafloor. TD = total depth.

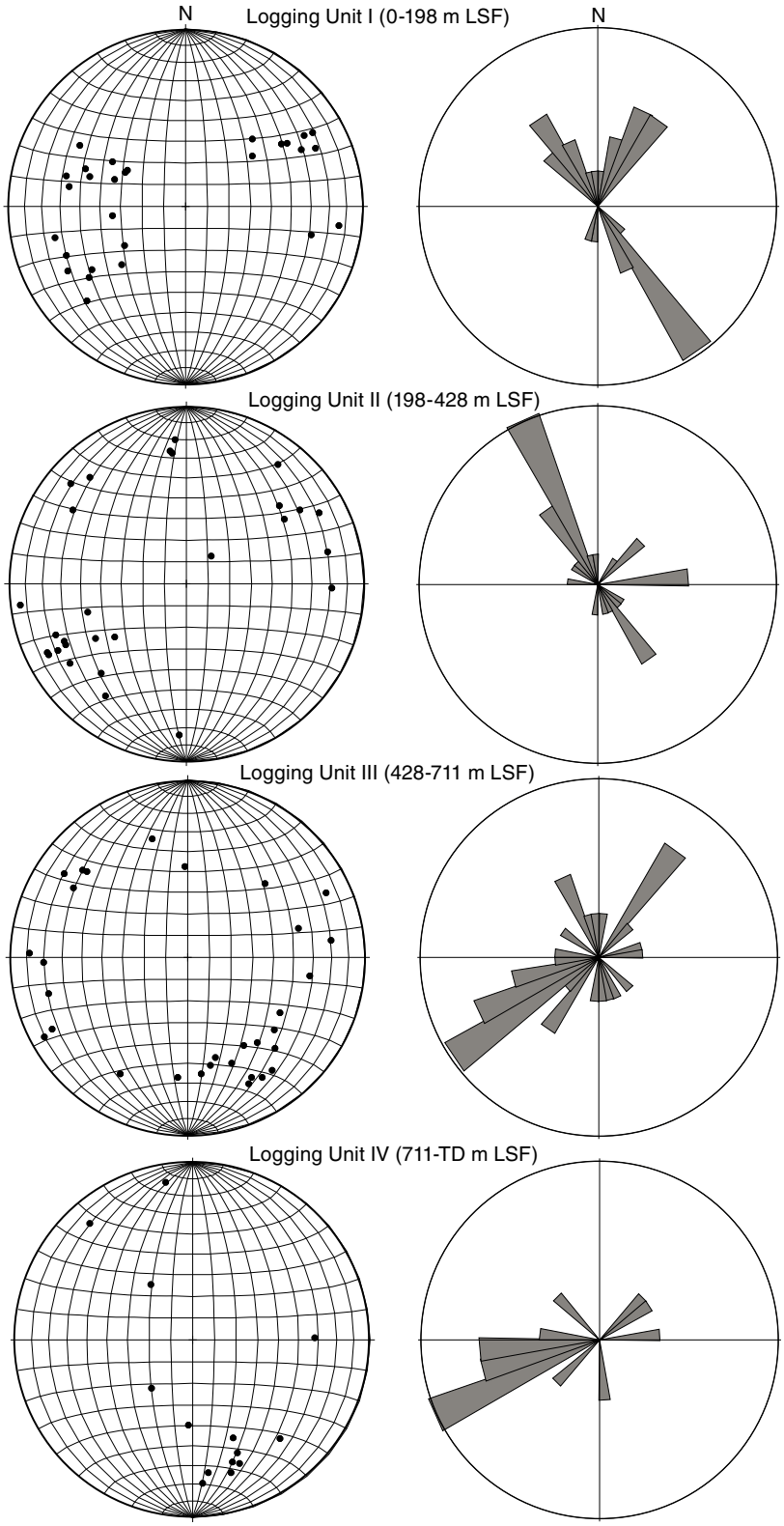

Figure F25. Distribution of borehole breakout azimuths and widths. **A.** Histogram of breakout azimuths. **B.** Variation of breakout azimuths with depth. **C.** Histogram of breakout widths. **D.** Variation of breakout widths with depth. Note decreasing width with depth. LSF = LWD depth below seafloor.

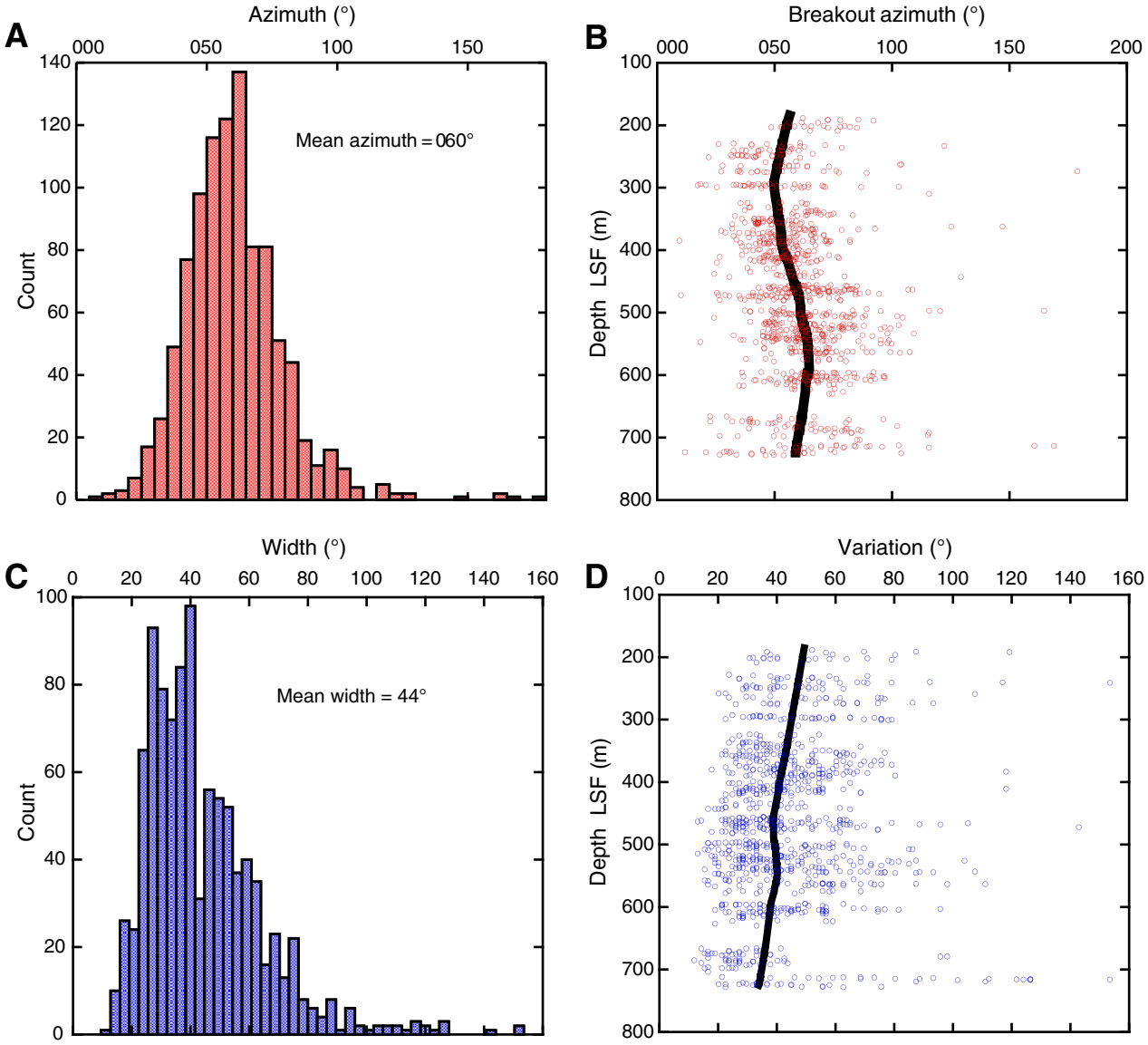

Figure F26. Orientation of S_{Hmax}. Note consistency of trend across accretionary prism at Sites C0006, C0004, and C0001 and contrasting orientation in forearc basin at Site C0002. Orientations at Site C0002 represent change in S_{Hmax} from shallow depths in forearc basin (red lines) to near base of hole in underlying accretionary prism (blue line). Convergence vector represents range from Miyasaki and Heki (2001), Heki (2007), and Seno et al. (1993). GPS = Global Positioning System.

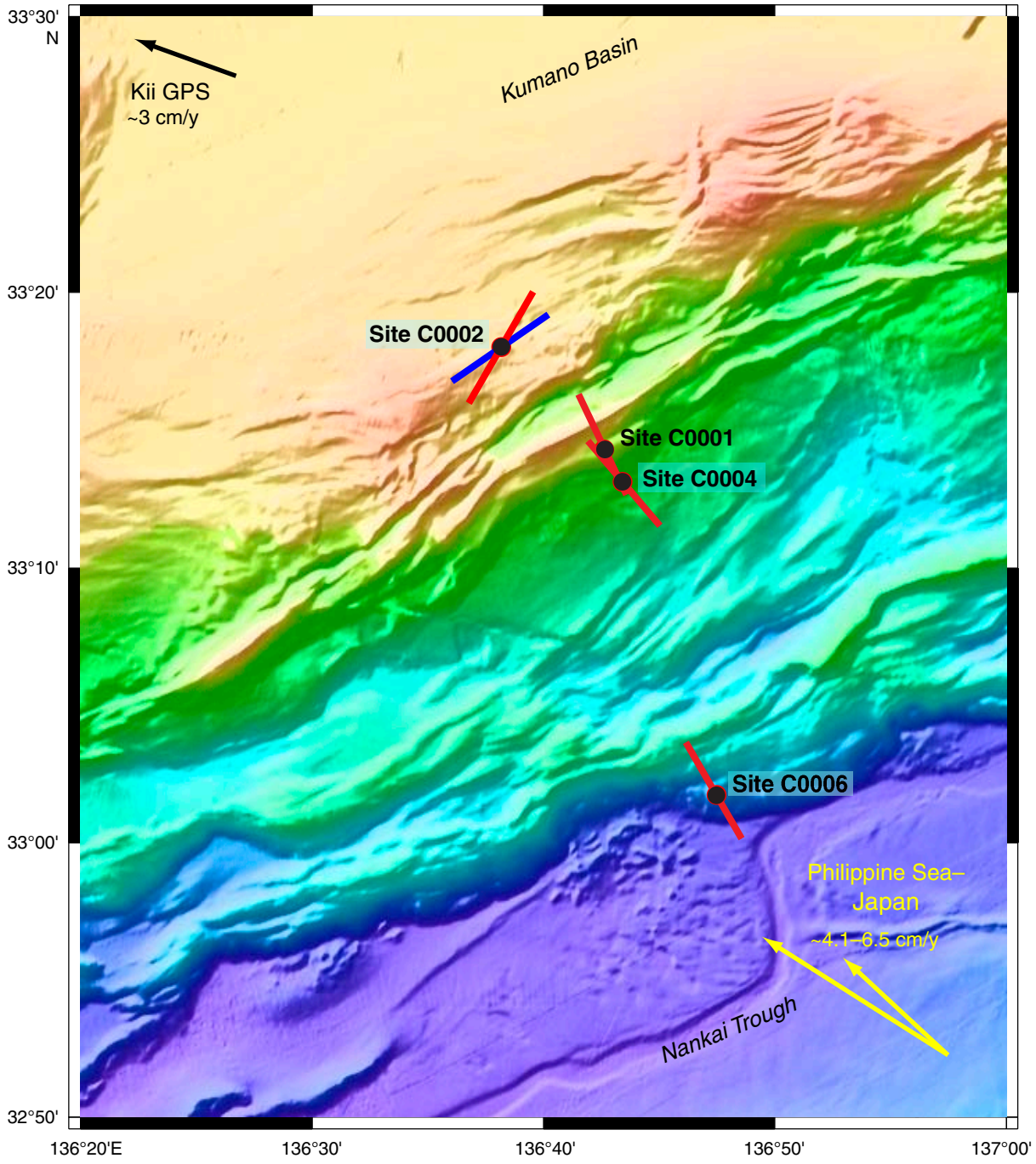

Figure F27. Seismic reflection section (check shot–corrected depth section for prestack depth-migrated Inline 2434), Site C0006. **A.** Uninterpreted (red = positive amplitudes, black = negative amplitudes). **B.** Interpreted (black = positive amplitudes, white = negative amplitudes). Red = thrust faults (with the main frontal thrust being the deepest fault), blue and yellow = key reflections correlated with features in the LWD data. VE = vertical exaggeration.

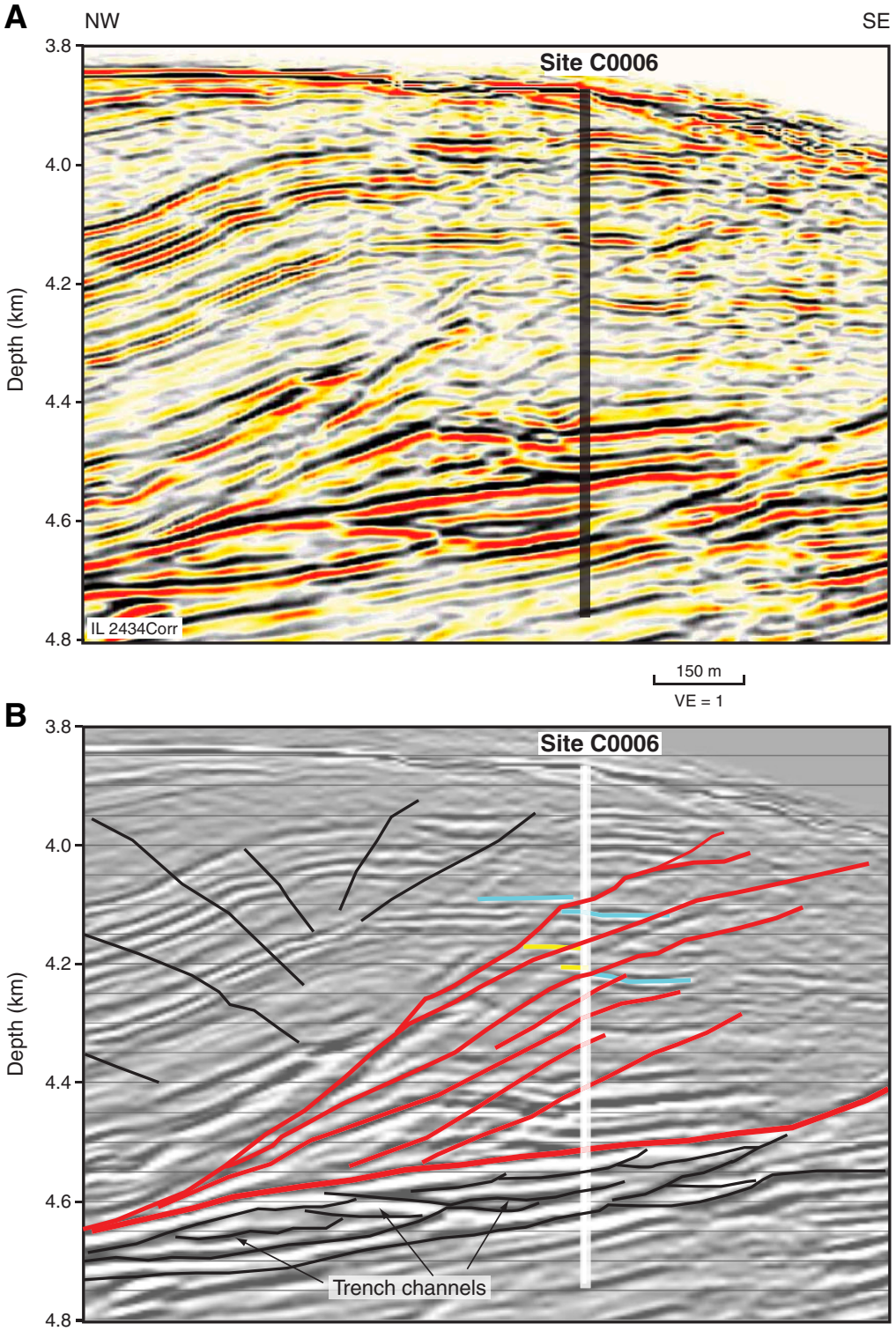

Figure F28. Check shot display showing clear first arrivals from seismicVISION tool. LSF = LWD depth below seafloor.

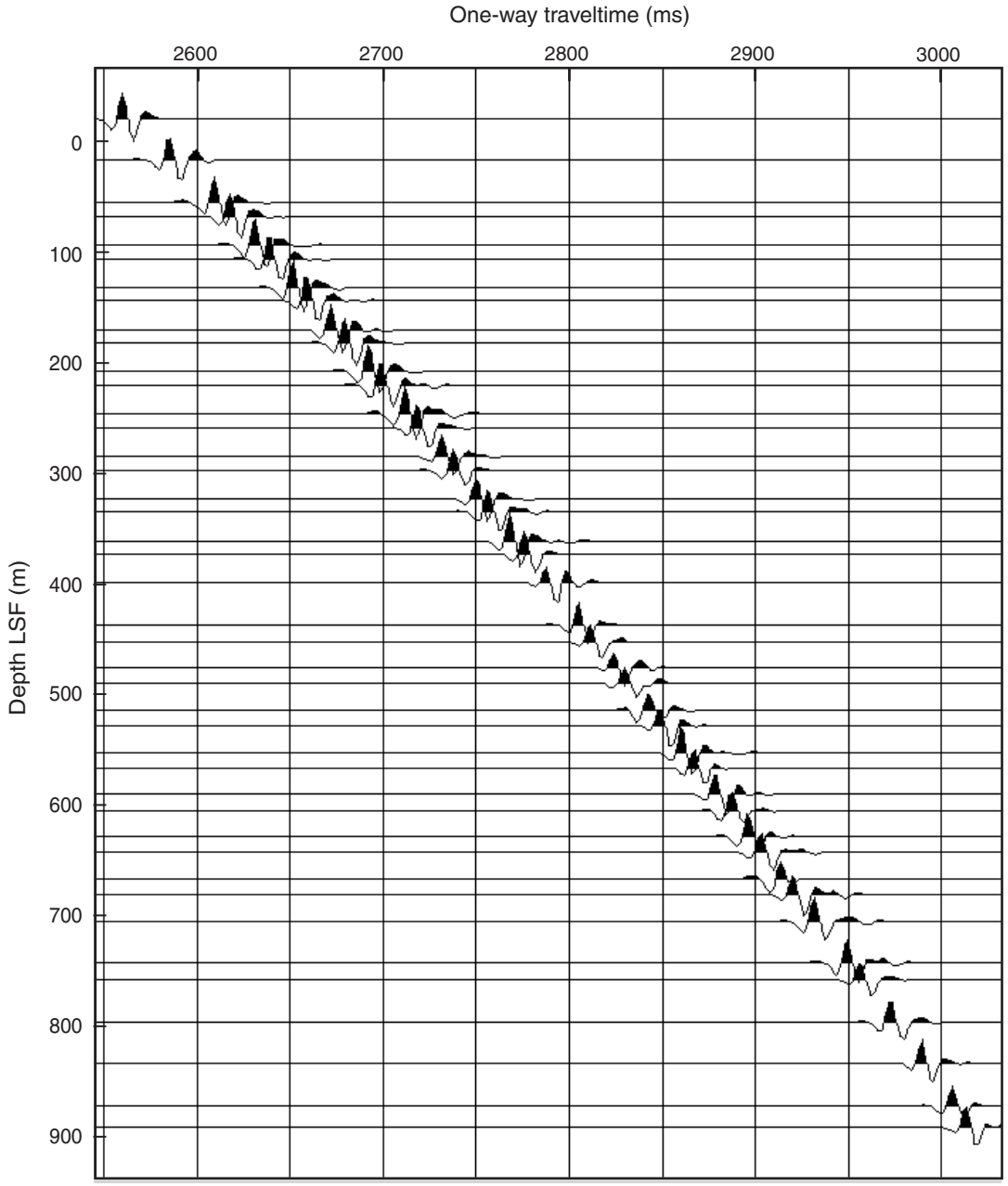

Figure F29. Smoothed and raw check shot interval velocities. LSF = LWD depth below seafloor.

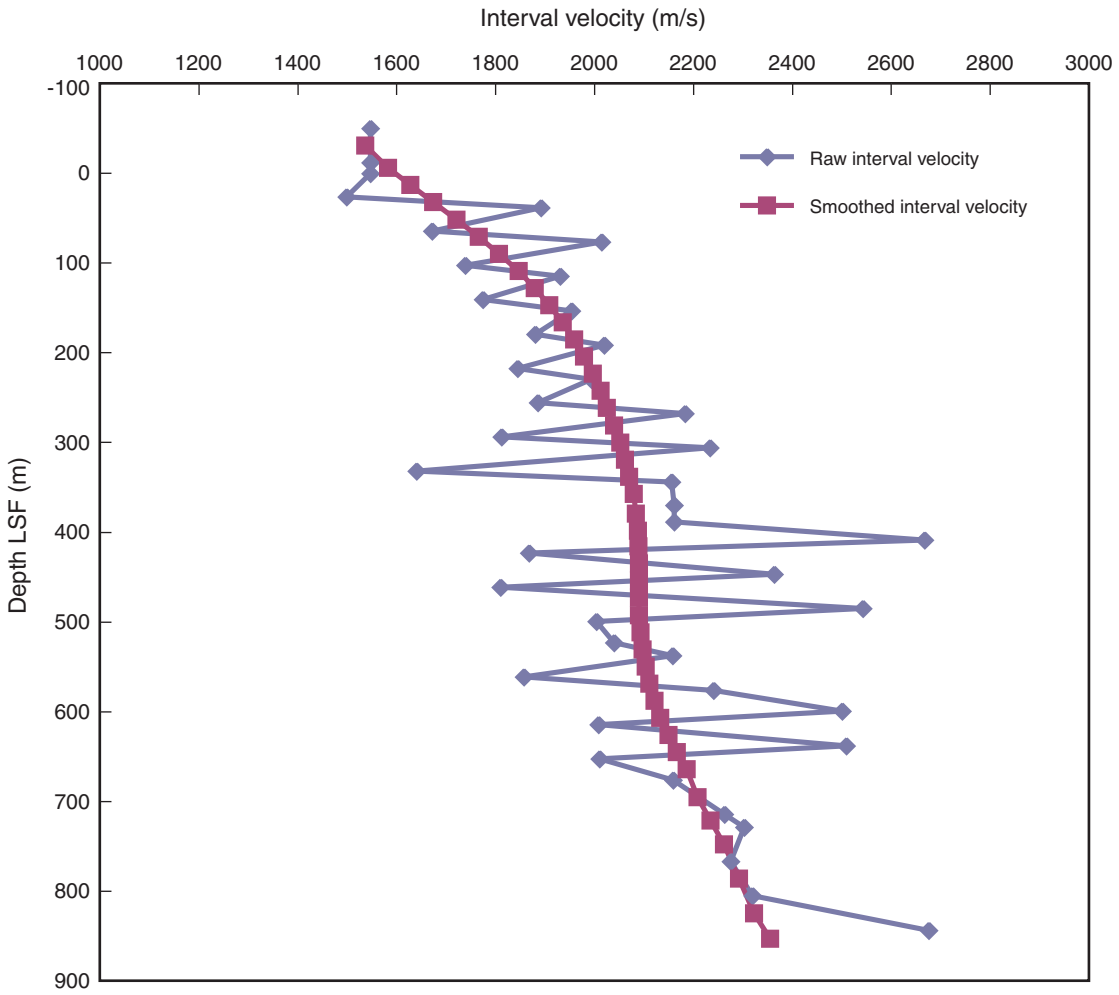

Figure F30. Logging units and subunits superimposed on check shot–corrected seismic profile. LSF = LWD depth below seafloor. VE = vertical exaggeration.

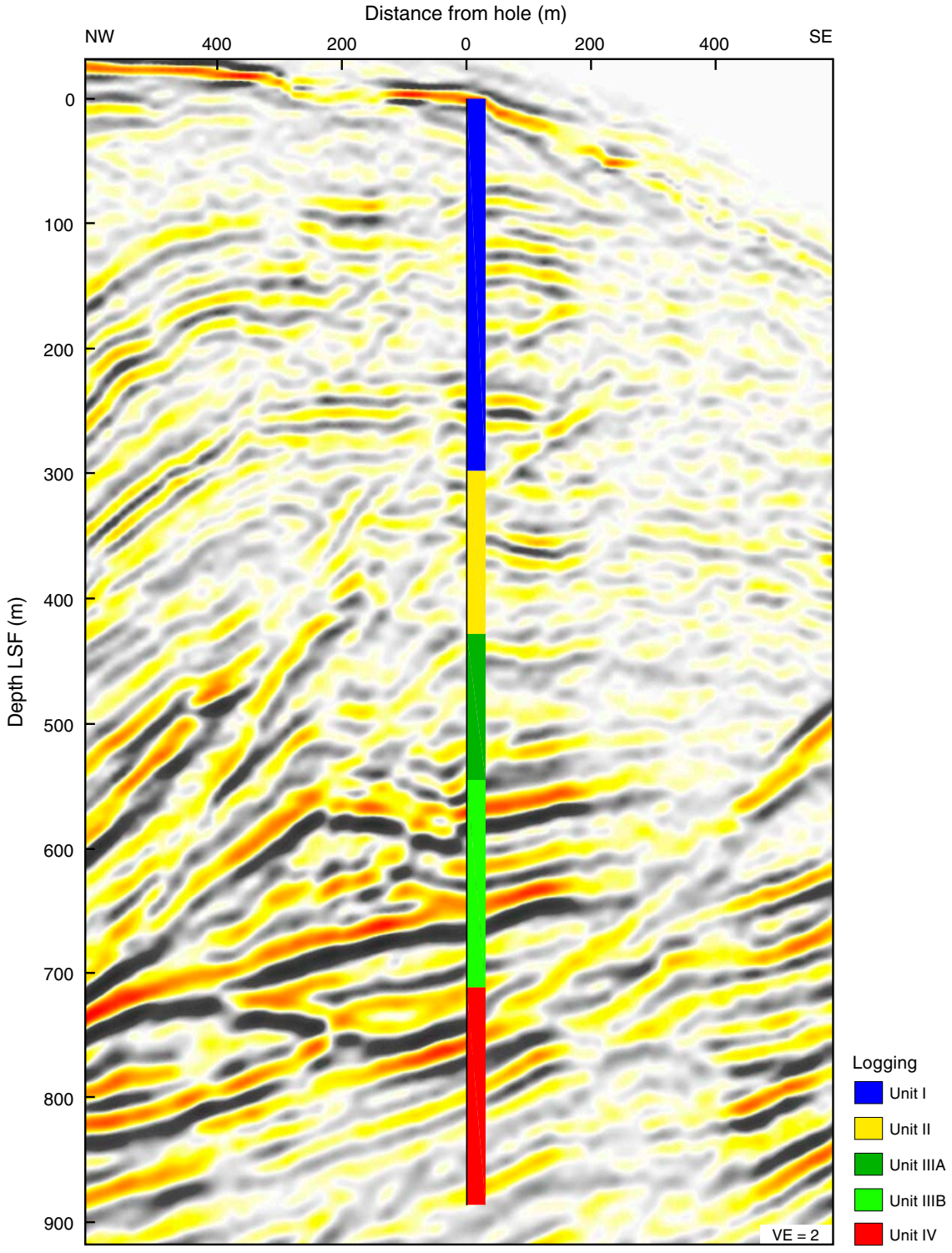

Figure F31. LWD gamma ray log superimposed on check shot–corrected seismic profile. LSF = LWD depth below seafloor. VE = vertical exaggeration.

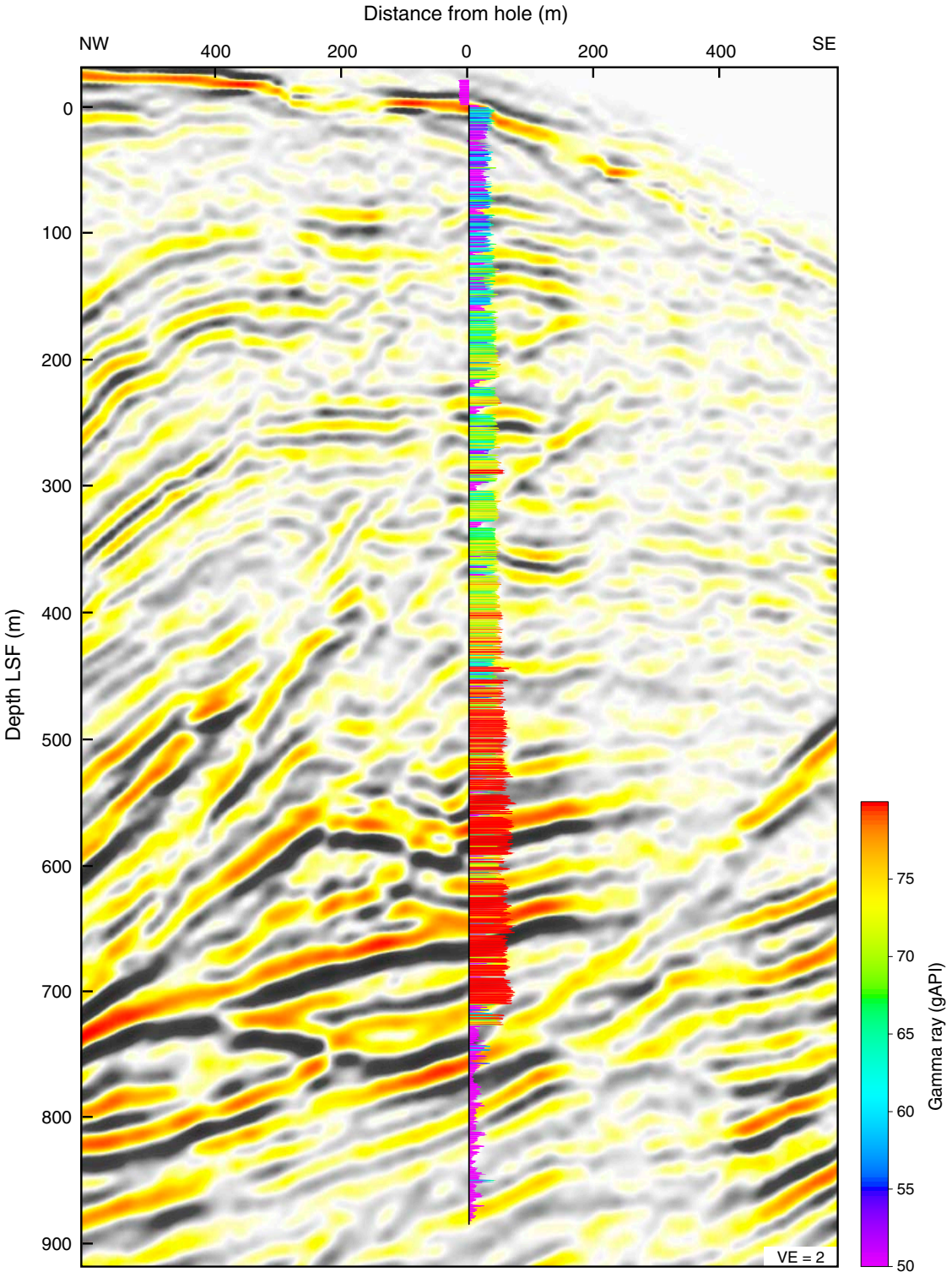

Figure F32. LWD bit resistivity superimposed on check shot–corrected seismic profile. LSF = LWD depth below seafloor. VE = vertical exaggeration.

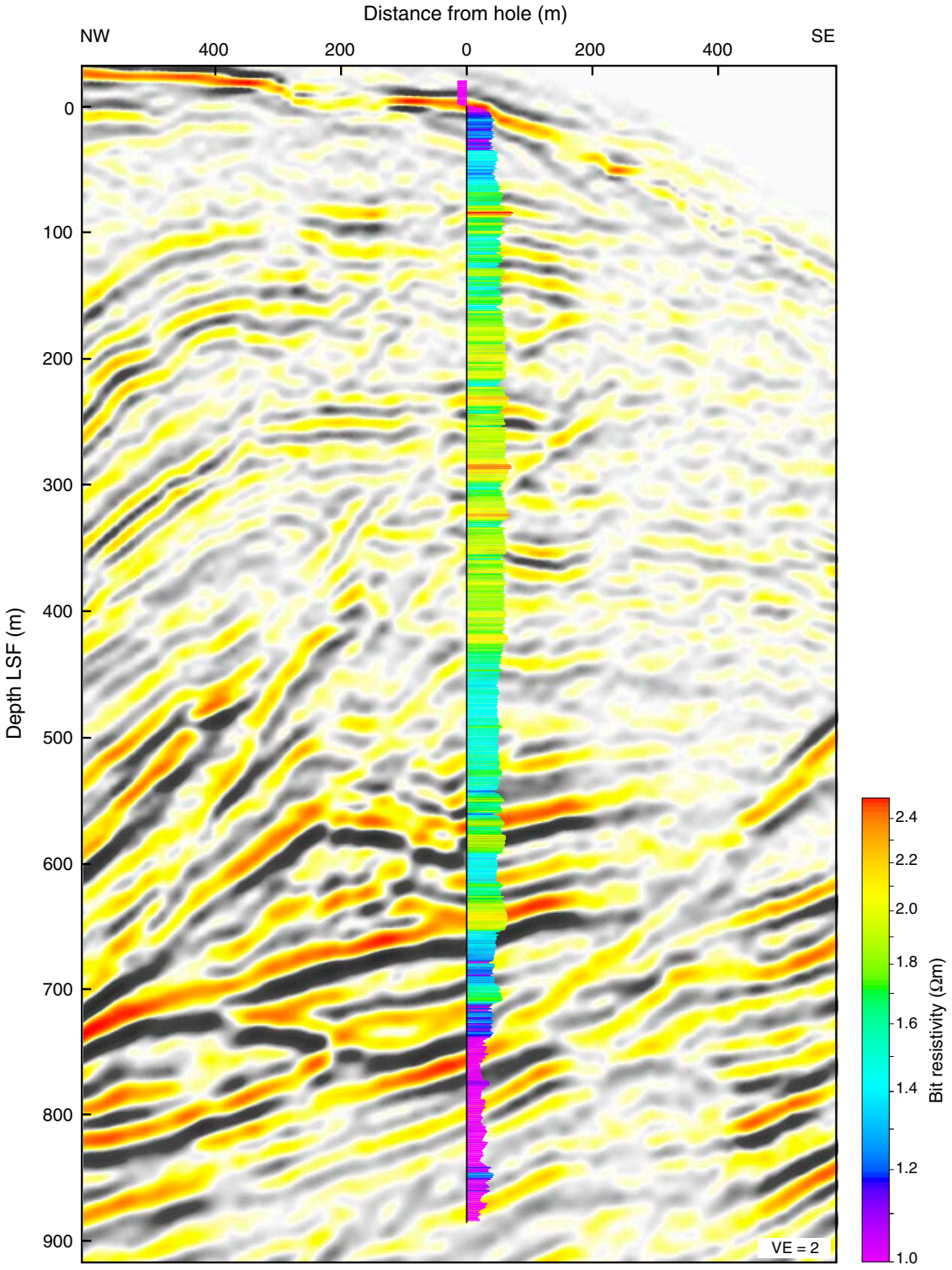

Figure F33. LWD ring resistivity superimposed on check shot–corrected seismic profile. LSF = LWD depth below seafloor. VE = vertical exaggeration.

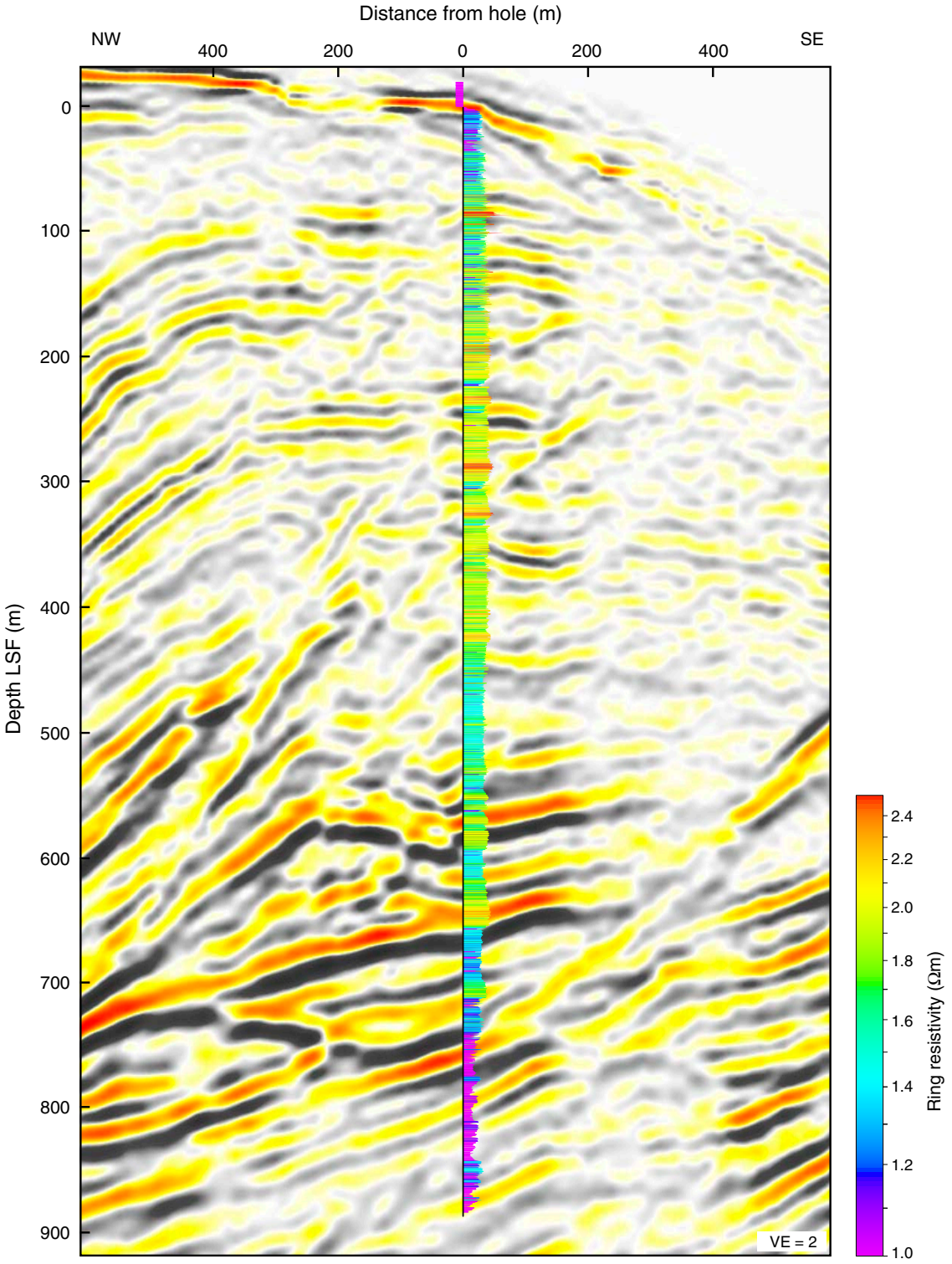

Figure F34. LWD caliper values superimposed on check shot–corrected seismic profile. LSF = LWD depth below seafloor. VE = vertical exaggeration.

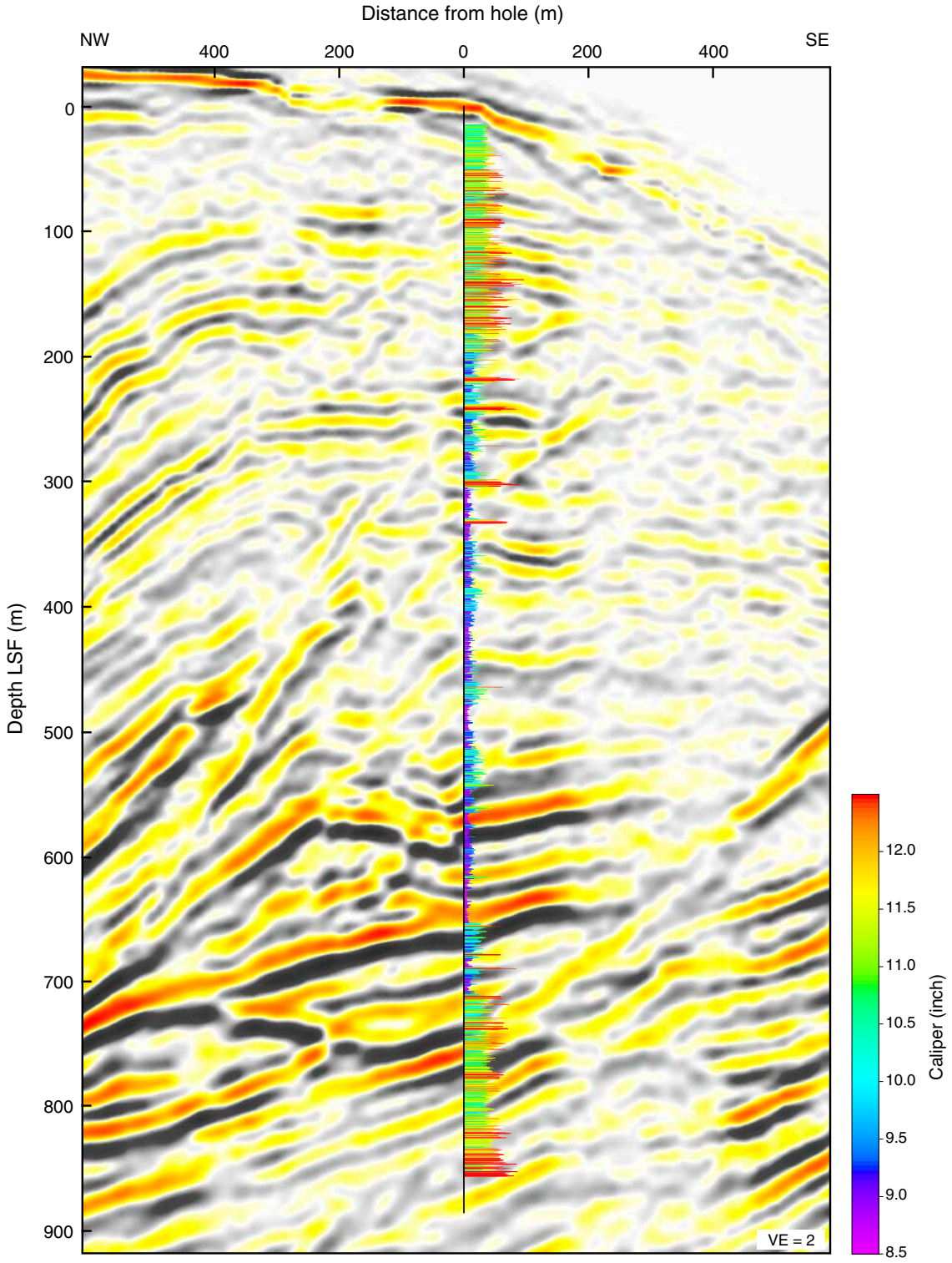

Table T1. Operations summary, Site C0006. (See table notes.)

Hole C0006A
Latitude: 33°01.6430′N
Longitude: 136°47.6550′E
Seafloor (drill pipe measurement from rig floor, m): 3903.5
Distance between rig floor and sea level (m): 28.5
Water depth (drill pipe measurement from sea level, m): 3875

Hole C0006B
Latitude: 33°01.6350′N
Longitude: 136°47.6390′E
Seafloor (drill pipe measurement from rig floor, m): 3900
Distance between rig floor and sea level (m): 28.5
Water depth (drill pipe measurement from sea level, m): 3871.5

Operation	Start Date (2007)	Start Local time (h)	Depth (m LSF) Top	Depth (m LSF) Bottom	Drilled (m LSF)	Comments
Hole C0006A pilot hole			0	885.5	885.5	8-1/2 inch pilot hole with MWD-GR-APWD
ROV survey	8 Nov	0415				Deploy 5 beacons with ROV
Spud-in	10 Nov	0015				Jet-in to 50.5 m LSF; rotary drilling continued to TD
Ream and sweep	10 Nov	1415				Short trip from 4210 to 4060 m DRF
Ream and sweep	11 Nov	0500				Short trip from 4504 to 4358 m DRF
Reach total depth	11 Nov	1045	0			Pump sweep and spot kill mud
Pull tools out of hole	11 Nov	2045				Check and tighten rig floor instruments while pulling out
Hole C0006B LWD hole			0	885.5	885.5	8-1/2 inch LWD (GVR-sonic-SVWD-MWD-APWD)
ROV survey	13 Nov	0045				
Spud-in	13 Nov	0045				Jet-in to 40 m LSF and rotary drill to TD
Rig floor maintenance	13 Nov	1400				No real-time data, lost communication from MWD tool
Ream and sweep	14 Nov	0315				Wiper trip between 4502 and 4350 m DRF
Reach total depth	14 Nov	1645				Pump sweep and spot kill mud
Pull tools out of hole	14 Nov	1900				Pump and backream because of hole sticky condition
Recover tools on the rig floor	15 Nov	1715				
Recover data	15 Nov	1900				Download data

Notes: LSF = LWD depth below seafloor. ROV = remotely operated vehicle. MWD = measurement while drilling, GR = gamma ray, APWD = annular pressure while drilling. TD = total depth. DRF = drillers depth below rig floor. LWD = logging while drilling, GVR = geoVISION resistivity tool, sonic = sonic while drilling (sonicVISION), SVWD = seismicVISION while drilling, MWD = measurement while drilling.

Table T2. Bottom-hole assembly, Hole C0006A. (See table notes.)

BHA component	Length (m)	Cumulative length from bit (m)
PDC bit	0.350	0.350
Stabilizer/float sub	0.610	0.960
Crossover sub	0.610	1.570
Power pulse	8.496	10.066
Crossover sub	0.480	10.546
Crossover sub	0.610	11.156
Crossover sub	0.610	11.766
6-3/4 inch drilling collar	9.310	21.076
Stabilizer	1.504	22.580
6-3/4 inch drilling collar	9.313	31.893
6-3/4 inch drilling collar	9.310	41.203
6-3/4 inch drilling collar	9.292	50.495
6-3/4 inch drilling collar	9.312	59.807
6-3/4 inch drilling collar	9.314	69.121
6-3/4 inch drilling collar	9.310	78.431
6-3/4 inch drilling collar	9.316	87.747
Jar	10.215	97.962
6-3/4 inch drilling collar	9.314	107.276
Crossover sub	0.611	107.887
Crossover sub	0.605	108.492

Notes: BHA = bottom-hole assembly. PDC = polycrystalline diamond compact.

Table T3. Bottom-hole assembly, Hole C0006B. (See table notes.)

BHA component	Length (m)	Cumulative length from bit (m)
PDC bit	0.350	0.350
Stabilizer/float sub	0.610	0.960
Crossover sub	0.615	1.575
geoVISION	3.084	4.659
sonicVISION	7.624	12.283
Power pulse	8.496	20.779
seismicVISION	4.640	25.419
adnVISION	6.098	31.517
Crossover sub	0.610	32.127
6-3/4 inch drilling collar	9.310	41.437
6-3/4 inch drilling collar	9.313	50.750
6-3/4 inch drilling collar	9.310	60.060
6-3/4 inch drilling collar	9.292	69.352
6-3/4 inch drilling collar	9.312	78.664
6-3/4 inch drilling collar	9.314	87.978
6-3/4 inch drilling collar	9.310	97.288
6-3/4 inch drilling collar	9.316	106.604
Jar	10.215	116.819
6-3/4 inch drilling collar	9.310	126.129
Crossover sub	0.611	126.740
Crossover sub	0.605	127.345

Notes: BHA = bottom-hole assembly. PDC = polycrystalline diamond compact.

Table T4. Quality control characteristics and sonic log data, Hole C0006B. (See table notes.)

Depth interval (m LSF)				
Top	Bottom	Zone	Quality	Comments
0	36	1	0	Formation arrival cannot be distinguished from the mud arrival
36	160	1	1	Fairly intermittent arrivals with zones of clear arrivals and zones hard to pick up on MP wide

Notes: LSF = LWD depth below seafloor. MP = mixed processing (see "Data and log quality").

Table T5. Quality control characteristics and resistivity image data, Hole C0006B. (See table note.)

Depth interval (m LSF)		
Top	Bottom	Comments
40	69	Resistivity variation on 180° frequency, probably due to hole enlargement and eccentricity of tool relative to borehole wall.
420	445	Meter-scale spiral banding, suspected tool artifact.
480	520	Meter-scale spiral banding, suspected tool artifact.
520	595	Meter-scale spiral banding, suspected tool artifact.
619	633	Meter-scale spiral banding, suspected tool artifact.
733	819	Resistivity variation on 180° frequency, probably due to hole enlargement and eccentricity of tool relative to borehole wall.
40	885	Centimeter-scale horizontal banding, suspected tool artifact, tends to obscure shallowly dipping bedding and fractures.

Note: LSF = LWD depth below seafloor.

Table T6. Logging units defined by LWD data. (See table note.)

Logging Unit	Subunit	Depth (m LSF)	Description	Lithologic interpretation
I		0–197.8	Gamma ray increasing trend, high-frequency and high-amplitude fluctuation of gamma ray values. Gradual increasing trend of resistivity. Strong fluctuation of resistivity.	Sandy and muddy sediments
II		197.8–428.3	Gradual increasing trend of gamma ray baseline. Occasional thick (5 m) low gamma ray layers. Constant resistivity baseline with frequent thick conductive zones.	Mudstone with thick sand
III	A	428.3–545.3	High gamma ray baseline with thin (1 m) low gamma ray layers. Less variable and slight decreasing trend of resistivity.	Alternating beds of mudstone and sand (mud dominant)
	B	545.3–711.5	High gamma ray baseline with large number of thin (1 m) low gamma ray layers. General decreasing and variable (repeated increasing) trend of resistivity.	Alternating beds of mudstone and sand (sand dominant)
IV		711.5–TD	Low gamma ray and low resistivity.	Sand

Note: LSF = LWD depth below seafloor. TD = total depth.

Table T7. Logging unit boundaries defined by LWD data. (See table note.)

Depth (m LSF)	Unit boundary		Description
79.8	Minor		Low-amplitude to high-amplitude fluctuation of gamma ray. End of increasing trend of resistivity.
146.1	Minor		High-amplitude to low-amplitude fluctuation of gamma ray.
197.8	Medium	I/II	High-frequency and high-amplitude to low-frequency and low-amplitude fluctuation of resistivity.
293.0	Minor		Baseline shift of resistivity.
428.3	Medium	II/III	Baseline shift of resistivity.
545.3	Medium	IIIA/IIIB	High-frequency to low-frequency fluctuation of gamma ray. Constant to variable values of resistivity.
593.4	Medium		Baseline shift of gamma ray, resistivity, and caliper.
657.0	Medium		Baseline shift of resistivity and caliper.
711.5	Major	III/IV	Strong baseline shift of gamma ray. Baseline shift of resistivity and caliper.
764.4	Medium		High-frequency to low-frequency fluctuation of resistivity.

Note: LSF = LWD depth below seafloor.

Table T8. Check shot raw and smoothed traveltimes and calculated interval velocities, Site C0006. (**See table notes.**)

Depth* (m LSF)	Midpoint depth† (m LSF)	Raw		Smoothed	
		First arrival time* (ms)	Interval velocity† (m/s)	First arrival time* (ms)	Interval velocity† (m/s)
–49.98	–30.86	2556.8	1547	2556.9	1537
–11.75	–5.65	2581.5	1547	2581.8	1582
0.45	13.46	2589.4	1548	2589.5	1628
26.47	32.57	2606.2	1499	2605.5	1674
38.68	51.69	2614.3	1892	2612.8	1721
64.70	70.80	2628.1	1672	2627.9	1766
76.90	89.91	2635.4	2015	2634.8	1807
102.92	109.02	2648.3	1739	2649.2	1847
115.12	128.13	2655.3	1931	2655.8	1880
141.14	147.24	2668.8	1775	2669.6	1909
153.35	166.37	2675.7	1954	2676.0	1936
179.40	185.47	2689.0	1880	2689.5	1959
191.54	204.58	2695.5	2020	2695.7	1979
217.62	223.71	2708.4	1845	2708.9	1997
229.79	242.80	2715.0	1993	2715.0	2012
255.81	261.90	2728.0	1886	2727.9	2025
267.99	281.01	2734.5	2184	2733.9	2040
294.04	300.14	2746.4	1812	2746.7	2052
306.24	319.25	2753.1	2233	2752.6	2062
332.26	338.36	2764.8	1641	2765.2	2070
344.47	357.48	2772.2	2156	2771.1	2079
370.48	379.61	2784.3	2162	2783.6	2084
388.73	398.72	2792.7	2161	2792.4	2088
408.71	416.01	2802.0	2668	2802.0	2090
423.31	435.10	2807.5	1868	2809.0	2090
446.90	454.20	2820.1	2364	2820.2	2090
461.50	473.31	2826.3	1810	2827.2	2090
485.12	492.44	2839.3	2543	2838.5	2090
499.76	511.57	2845.1	2004	2845.5	2093
523.38	530.68	2856.9	2040	2856.8	2097
537.98	549.79	2864.0	2158	2863.8	2103
561.60	568.90	2875.0	1858	2875.0	2112
576.20	588.00	2882.8	2241	2881.9	2122
599.79	607.11	2893.3	2501	2893.0	2134
614.43	626.22	2899.2	2008	2899.9	2150
638.02	645.32	2910.9	2509	2910.9	2167
652.62	664.43	2916.8	2011	2917.6	2187
676.24	695.32	2928.5	2159	2928.4	2209
714.40	721.71	2946.2	2263	2945.7	2235
729.03	748.14	2952.7	2303	2952.2	2262
767.26	786.38	2969.2	2276	2969.1	2292
805.51	824.64	2986.1	2320	2985.8	2322
843.77	853.43	3002.6	2677	3002.3	2355
863.09	—	3009.8	—	3010.5	—

Notes: Smoothed values were used in the generation of synthetic seismograms and time-depth conversion of seismic reflection profiles near the site. * = first arrival time picks associated with depths of observations, † = interval velocities associated with midpoints between depths of observations. LSF = LWD depth below seafloor. — = no data.